Astronomy & Astrophysics manuscript no. bonaldi˙v4.5
January 25, 2013

Planck intermediate results. XII: Diffuse Galactic components in the Gould Belt System

Planck Collaboration: P. A. R. Ade[75], N. Aghanim[51], M. I. R. Alves[51], M. Arnaud[65], M. Ashdown[61,6], F. Atrio-Barandela[18], J. Aumont[51], C. Baccigalupi[74], A. J. Banday[80,9], R. B. Barreiro[58], J. G. Bartlett[1,59], E. Battaner[82], L. Bedini[8], K. Benabed[52,79], A. Benoît[49], J.-P. Bernard[9], M. Bersanelli[30,43], A. Bonaldi⋆[60], J. R. Bond[7], J. Borrill[13,76], F. R. Bouchet[52,79], F. Boulanger[51], C. Burigana[42,28], R. C. Butler[42], X. Chen[48], L.-Y Chiang[54], P. R. Christensen[72,33], D. L. Clements[47], S. Colombi[52,79], L. P. L. Colombo[23,59], A. Coulais[64], F. Cuttaia[42], R. D. Davies[60], R. J. Davis[60], P. de Bernardis[29], G. de Zotti[38,74], J. Delabrouille[1], C. Dickinson[60], J. M. Diego[58], G. Dobler[62], H. Dole[51,50], S. Donzelli[43], O. Doré[59,10], M. Douspis[51], X. Dupac[35], T. A. Enßlin[69], F. Finelli[42,44], O. Forni[80,9], M. Frailis[40], E. Franceschi[42], S. Galeotta[40], K. Ganga[1], R. T. Génova-Santos[57], T. Ghosh[51], M. Giard[80,9], G. Giardino[36], Y. Giraud-Héraud[1], J. González-Nuevo[58,74], K. M. Górski[59,84], A. Gregorio[31,40], A. Gruppuso[42], F. K. Hansen[56], D. Harrison[55,61], C. Hernández-Monteagudo[12,69], S. R. Hildebrandt[10], E. Hivon[52,79], M. Hobson[6], W. A. Holmes[59], A. Hornstrup[16], W. Hovest[69], K. M. Huffenberger[83], T. R. Jaffe[80,9], A. H. Jaffe[47], M. Juvela[24], E. Keihänen[24], R. Keskitalo[21,13], T. S. Kisner[68], J. Knoche[69], M. Kunz[17,51,3], H. Kurki-Suonio[24,37], G. Lagache[51], A. Lähteenmäki[2,37], J.-M. Lamarre[64], A. Lasenby[6,61], C. R. Lawrence[59], S. Leach[74], R. Leonardi[35], P. B. Lilje[56,11], M. Linden-Vørnle[16], P. M. Lubin[25], J. F. Macías-Pérez[66], B. Maffei[60], D. Maino[30,43], N. Mandolesi[42,5,28], M. Maris[40], D. J. Marshall[65], P. G. Martin[7], E. Martínez-González[58], S. Masi[29], M. Massardi[41], S. Matarrese[27], P. Mazzotta[32], A. Melchiorri[29,45], A. Mennella[30,43], S. Mitra[46,59], M.-A. Miville-Deschênes[51,7], A. Moneti[52], L. Montier[80,9], G. Morgante[42], D. Mortlock[47], D. Munshi[75], J. A. Murphy[71], P. Naselsky[72,33], F. Nati[29], P. Natoli[28,4,42], H. U. Nørgaard-Nielsen[16], F. Noviello[60], D. Novikov[47], I. Novikov[72], S. Osborne[78], C. A. Oxborrow[16], F. Pajot[51], R. Paladini[48], D. Paoletti[42,44], M. Peel[60], L. Perotto[66], F. Perrotta[74], F. Piacentini[29], M. Piat[1], E. Pierpaoli[23], D. Pietrobon[59], S. Plaszczynski[63], E. Pointecouteau[80,9], G. Polenta[4,39], L. Popa[53], T. Poutanen[37,24,2], G. W. Pratt[65], S. Prunet[52,79], J.-L. Puget[51], J. P. Rachen[20,69], W. T. Reach[81], R. Rebolo[57,14,34], M. Reinecke[69], C. Renault[66], S. Ricciardi[42], I. Ristorcelli[80,9], G. Rocha[59,10], C. Rosset[1], J. A. Rubiño-Martín[57,34], B. Rusholme[48], E. Salerno[8], M. Sandri[42], G. Savini[73], D. Scott[22], L. Spencer[75], V. Stolyarov[6,61,77], R. Sudiwala[75], A.-S. Suur-Uski[24,37], J.-F. Sygnet[52], J. A. Tauber[36], L. Terenzi[42], C. T. Tibbs[48], L. Toffolatti[19,58], M. Tomasi[43], M. Tristram[63], L. Valenziano[42], B. Van Tent[67], J. Varis[70], P. Vielva[58], F. Villa[42], N. Vittorio[32], L. A. Wade[59], B. D. Wandelt[52,79,26], N. Ysard[24], D. Yvon[15], A. Zacchei[40], and A. Zonca[25]

(Affiliations can be found after the references)

Preprint online version: January 25, 2013

ABSTRACT

We perform an analysis of the diffuse low-frequency Galactic components in the Southern part of the Gould Belt system ($130^\circ \le l \le 230^\circ$ and $-50^\circ \le b \le -10^\circ$). Strong UV flux coming from the Gould Belt super-association is responsible for bright diffuse foregrounds that we observe from our position inside the system and that can help us improve our knowledge of the Galactic emission. Free-free emission and anomalous microwave emission (AME) are the dominant components at low frequencies ($\nu < 40$ GHz), while synchrotron emission is very smooth and faint. We separate diffuse free-free emission and AME from synchrotron emission and thermal dust emission by using *Planck* data, complemented by ancillary data, using the "Correlated Component Analysis" (CCA) component separation method and we compare with the results of cross-correlation of foreground templates with the frequency maps. We estimate the electron temperature T_e from Hα and free-free emission using two methods (temperature-temperature plot and cross-correlation) and we consistently obtain T_e ranging from 7000 to 2000 K for a dust absorption fraction of f_d = 0–0.5. We estimate the frequency spectrum of the diffuse AME and we recover a peak frequency (in flux density units) of 25.5 ± 1.5 GHz. We verify the reliability of this result with realistic simulations that include the presence of biases in the spectral model for the AME and in the free-free template. By combining physical models for vibrational and rotational dust emission and adding the constraints from the thermal dust spectrum from *Planck* and *IRAS* we are able to get a good description of the frequency spectrum of the AME for plausible values of the local density and radiation field.

Key words. Galaxy: general – radio continuum: ISM – radiation mechanisms: general

1. Introduction

The wide frequency coverage of the *Planck*[1] data gives a unique opportunity to study the main four Galactic foregrounds, namely free-free emission, synchrotron emission, anomalous microwave emission (AME) and thermal (vibrational) dust emission. The different frequency spectra of the components and their different spatial morphologies provide a means for separating the emission components. In this paper we apply the Correlated Component Analysis method (CCA, Bonaldi et al. 2006, Ricciardi et al. 2010), which uses the spatial morphology of the components to perform the separation. The local Gould Belt system of current star formation is chosen as a particularly interesting area in which to make an accurate separation of the four foregrounds because of the different morphologies of

⋆ Corresponding Author: A. Bonaldi anna.bonaldi@manchester.ac.uk

[1] *Planck* (http://www.esa.int/*Planck*) is a project of the European Space Agency (ESA) with instruments provided by two scientific consortia funded by ESA member states (in particular the lead countries France and Italy), with contributions from NASA (USA) and telescope reflectors provided by a collaboration between ESA and a scientific consortium led and funded by Denmark.

the components. Gould (1879) first noted this concentration of prominent OB associations inclined at 20° to the Galactic plane. It was next identified as an H I feature (Davies 1960, Lindblad 1967). Along with velocity data from H I and CO combined with stellar distances from *Hipparchos* the total system appears to be a slowly expanding and rotating ring of gas and dust surrounding a system of OB stars within 500 pc of the Sun (Lindblad et al. 1997). A recent modelling of the Gould Belt system by Perrot & Grenier (2003) gives semi-axes of 373×233 pc inclined at 17° with an ascending node at $l = 296°$ and a centre 104 pc distant from us lying at $l = 180°$. The Gould Belt thickness is 60 pc. The stars defining the system have ages less than 30×10^6 yr.

The free-free emission from ionized hydrogen is well-understood (Dickinson et al. 2003). Hα is a good indicator of the emission measure in regions of low dust absorption. Elsewhere a correction has to be applied, which depends on where the absorbing dust lies relative to the Hα emission. The conversion of an emission measure value to a radio brightness temperature at a given frequency requires a knowledge of the electron temperature. Alternatively, an electron temperature can be derived by assuming a value for the dust absorption. Values for the electron temperature of 4000–8000 K are found in similar studies (Banday et al. 2003, Davies et al. 2006, Ghosh et al. 2012). Radio recombination line observations on the Galactic plane (Alves et al. 2012) give values that agree with those of individual H II regions, having temperatures that rise with increasing distance from the Galactic centre; the value at the solar distance where the current study applies is 7000–8000 K.

The spectrum of synchrotron emission reflects the spectrum of the cosmic-ray electrons trapped in the Galactic magnetic field. At frequencies below a few GHz the brightness temperature spectral index, β_s, is ranging from −2.5 to −2.7 (Broadbent et al. 1989). Between 1.0 GHz and *WMAP* and *Planck* frequencies, the spectral index steepens to values from −2.9 to −3.1 (Banday et al. 2003, Davies et al. 2006, Kogut et al. 2011).

Thermal dust dominates the Galactic emission at *Planck* frequencies above 100 GHz. The spectrum is well-defined here with temperature $T_d \approx 18$ K and spectral index β_d ranging from 1.5 to 1.8 (Planck Collaboration XIX 2011). In the frequency range 60–143 GHz the dust emission overlaps that of the free-free emission and AME, making it a critical range for component separation.

The AME component is highly correlated with the far infrared dust emission (Kogut 1996, Leitch et al. 1997, Banday et al. 2003, Lagache 2003, de Oliveira-Costa et al. 2004, Finkbeiner et al. 2004, Davies et al. 2006, Dobler & Finkbeiner 2008a, Miville-Deschênes et al. 2008, Ysard et al. 2010, Gold et al. 2011, Planck Collaboration XX 2011) and is believed to be the result of electric dipole radiation from small spinning dust grains (Erickson 1957, Draine & Lazarian 1998) in a range of environments (Ali-Haïmoud et al. 2009, Ysard & Verstraete 2010). AME is seen in individual dust clouds associated with molecular clouds, photo-dissociation regions, reflection nebulae and H II regions (Planck Collaboration XX 2011). In the present study we will be examining the AME spectrum in more extended regions.

2. Definition of the region of interest and aim of the work

The projection of the Gould Belt disc on the sky is a strip that is superimposed on the Galactic plane, except towards the Galactic centre (Northern Gould Belt) and around $l = 180°$ (Southern Gould Belt). In this work we consider the Southern Gould Belt, which can be approximately defined by Galactic coordinates $130° \leq l \leq 230°$ and $-50° \leq b \leq -10°$ (see Fig. 1). This choice gives us a cleaner view of the Gould Belt, because the background emission from the Galactic Plane is weaker here than towards the Galactic centre. Notable structures within the region are the Orion complex, Barnard's arc and the Taurus, Eridanus, and Perseus star-forming complexes. All these emitting regions, including the diffuse emission from the Eridanus shell at $-50° < b < -30°$, are at a distance of approximately 500 pc from us and thus they belong to the local inter-stellar medium (ISM) associated with the Gould Belt (e.g. Reynolds & Ogden 1979, Boumis et al. 2001).

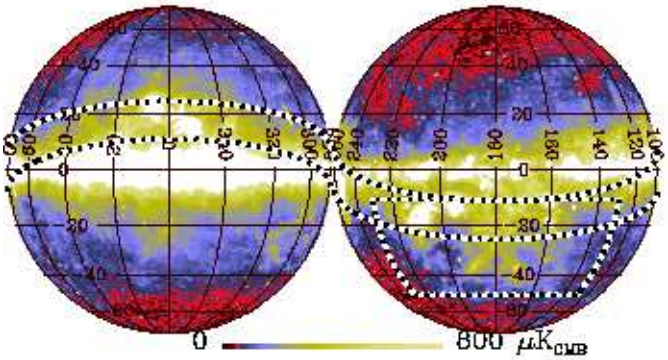

Fig. 1. Orthographic projection (looking towards the Galactic centre in the left panel and the Galactic anti-centre in the right panel) of the *Planck* CMB-subtracted 30 GHz channel showing the Gould Belt and the region of interest for this paper (defined by $130° \leq l \leq 230°$ and $-50° \leq b \leq -10°$).

In Fig. 2 we show the CMB-subtracted *Planck* data at 1° resolution, compared with the Haslam et al. (1982) 408 MHz map, which mostly traces the synchrotron component, the Dickinson et al. (2003) Hα map, tracing free-free emission, and the 100 μm map from Schlegel et al. (1998), tracing the dust emission. The visual inspection reveals dust-correlated features at low frequency, which could be attributed to AME. There is also prominent free-free emission, especially strong in the Barnard's arc region (towards $l = 207°, b = -18°$). The synchrotron component appears to be sub-dominant with respect to the free-free emission and the AME.

This work aims to separate and study the diffuse low-frequency foregrounds, in particular AME and free-free emission, in the region of interest. This requires the estimation of the spectral behaviour of the AME (carried out in Sect 4). We compare this spectrum with predictions for spinning dust emission, one of the mechanisms that is most often invoked to explain AME (Sect. 7). Having a reconstruction of the free-free emission, we estimate the free-free electron temperature (Sect. 6), which relates free-free brightness to emission measure, and investigate the dependence of this result on the dust absorption fraction.

3. Description of the analysis

3.1. Input data

Planck (Tauber et al. 2010; Planck Collaboration I 2011) is the third generation space mission to measure the anisotropy of the cosmic microwave background (CMB). It observes the sky in

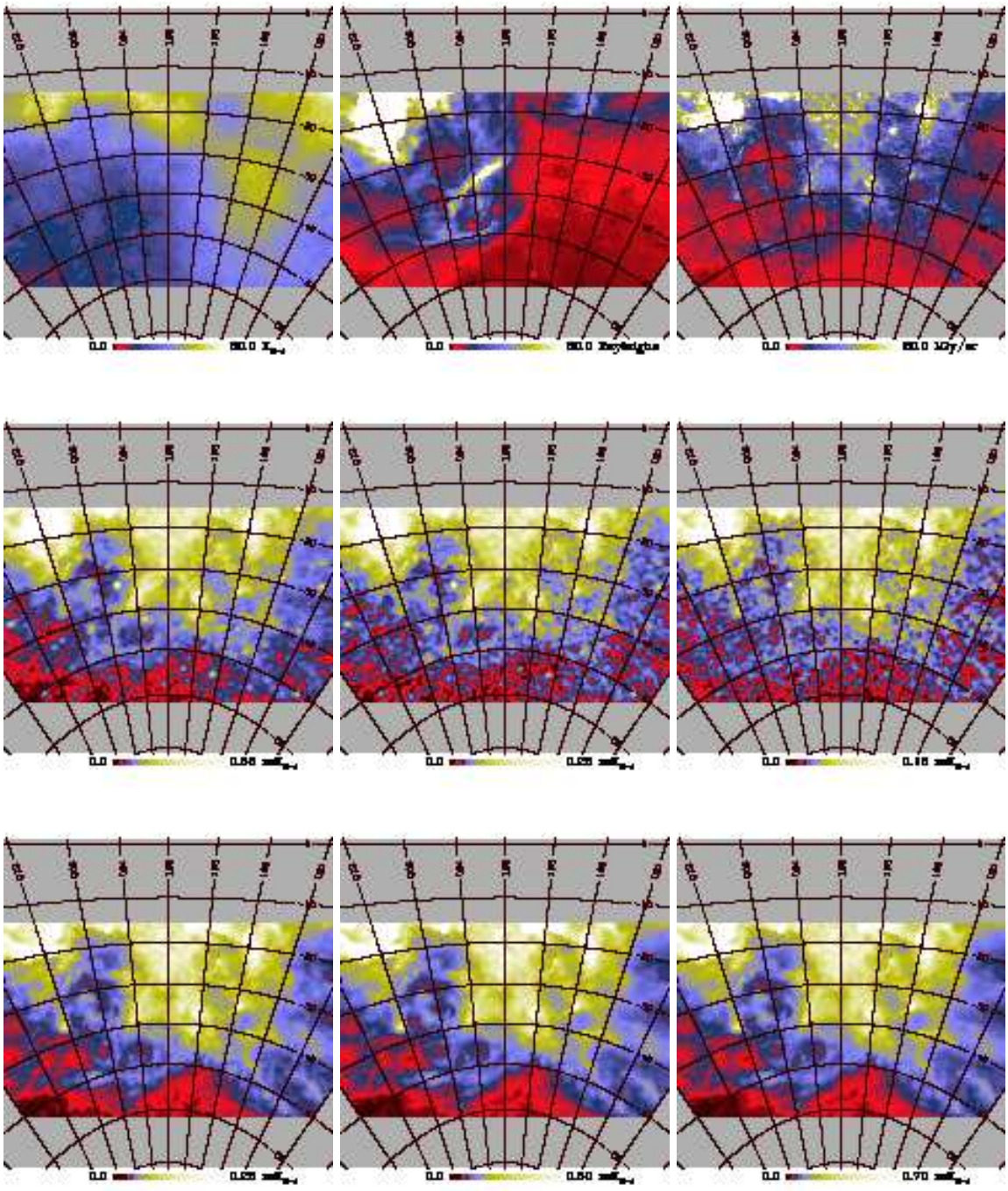

Fig. 2. Gnomonic projections of the region of interest. Top panels: Haslam et al. (1982) 408 MHz map (left); Hα map from Dickinson et al. (2003) (middle); and 100 μm map from Schlegel et al. (1998) (right) at native resolution. Middle panels (left to right): *Planck* CMB-subtracted 30, 44, and 70 GHz maps at 1° resolution. Bottom panels (left to right): *Planck* CMB-subtracted 143, 353, and 857 GHz at 1° resolution.

nine frequency bands covering 30–857 GHz with high sensitivity and angular resolution from 31′ to 5′. The Low Frequency Instrument (LFI; Mandolesi et al. 2010; Bersanelli et al. 2010; Mennella et al. 2011) covers the 30, 44, and 70 GHz bands with amplifiers cooled to 20 K. The High Frequency Instrument (HFI; Lamarre et al. 2010; Planck HFI Core Team 2011a) covers the 100, 143, 217, 353, 545, and 857 GHz bands with bolometers cooled to 0.1 K. Polarization is measured in all but the highest two bands (Leahy et al. 2010; Rosset et al. 2010). A combination of radiative cooling and three mechanical coolers produces the temperatures needed for the detectors and optics (Planck Collaboration II 2011). Two data processing centres (DPCs) check and calibrate the data and make maps of the sky (Planck HFI Core Team 2011b; Zacchei et al. 2011). *Planck*'s sensitivity, angular resolution, and frequency coverage make it a powerful instrument for galactic and extragalactic astrophysics as well as cosmology. Early astrophysics results are given in Planck Collaboration VIII–XXVI 2011, based on data taken between

Table 1. Summary of *Planck* data.

Central frequency [GHz]	Instrument	Resolution [arcmin]
28.5	*Planck* LFI	32.′65
44.1	*Planck* LFI	27.′92
70.3	*Planck* LFI	13.′01
100	*Planck* HFI	9.′88
143	*Planck* HFI	7.′18
217	*Planck* HFI	4.′87
353	*Planck* HFI	4.′65
545	*Planck* HFI	4.′72
857	*Planck* HFI	4.′39

13 August 2009 and 7 June 2010. Intermediate astrophysics results are now being presented in a series of papers based on data taken between 13 August 2009 and 27 November 2010.

The *Planck* data used throughout this paper are an internal data set known as DX7, whose properties are described in appendices to the LFI and HFI data processing papers (Planck Collaboration II 2013; Planck Collaboration VI 2013). However, we have tested the analysis to the extent that the results will not change if carried out on the maps which will be released to the public in March 2013.

The specifications of the *Planck* maps are reported in Table 1. The dataset used for the analysis consists of full resolution frequency maps and the corresponding noise information. We will indicate whenever the CMB-removed version of this dataset has been used for display purposes.

When analysing the results we apply a point source mask based on blind detection of sources above $5\,\sigma$ in each *Planck* map, as described in Zacchei et al. (2011) and Planck HFI Core Team (2011b). Ancillary data have been used throughout the paper for component separation purposes, to simulate the sky and data, or to analyse our results. The full list of ancillary data is reported in Table 2 with the main specifications.

3.2. Components

The main diffuse components present in the data are CMB and Galactic synchrotron emission, free-free emission, thermal dust emission, and anomalous microwave emission (AME). The frequency spectrum of the CMB component is well-known: it is accurately described by a black-body having temperature $T_{\rm CMB} = 2.7255\,K$ (Fixsen 2009).

Thermal dust emission dominates at high frequencies. Its spectral behaviour is a superposition of "grey-body" components identified by temperature $T_{\rm dust}$ and emissivity index $\beta_{\rm d}$:

$$T_{\rm RJ,dust}(\nu) \propto \nu^{\beta_{\rm d}+1}/[\exp(h\nu/kT_{\rm dust}) - 1], \quad (1)$$

where k is the Boltzmann constant and h is the Planck constant. In the approximation of a single component, over most of the sky we have $T_{\rm dust} \approx 18\,{\rm K}$ and $\beta_{\rm d}$ of 1.5–1.8 (Finkbeiner et al. 1999, Planck Collaboration XIX 2011, Planck Collaboration XXV 2011).

The frequency spectrum of the free-free component is often described by a power-law with spectral index −2.14 in RJ units. A more accurate description (see, e.g. Planck Collaboration XX 2011) is given by

$$T_{\rm RJ,ff}(\nu) \propto G(\nu) \times (\nu/10)^{-2}, \quad (2)$$

where $G = 3.96(T_4)^{0.21}(\nu/40)^{-0.14}$ is the Gaunt factor, which is responsible for the departure from a pure power-law behaviour. T_4 is the electron temperature $T_{\rm e}$ in units of $10^4\,{\rm K}$ ($T_{\rm e}$ can range over 2000–20000 K, but for most of the ISM it is 4,000–15,000 K).

The spectral behaviour of synchrotron radiation can be described to first order by a power-law model with spectral index $\beta_{\rm s}$ that typically assumes values from −2.5 to −3.2, depending on the position in the sky. Steepening of the synchrotron spectral index with frequency is expected due to energy losses of the electrons.

The frequency scaling of the AME component is the most poorly constrained. The distinctive feature is a peak around 20–40 GHz (Draine & Lazarian 1998, Dobler & Finkbeiner 2008b, Dobler et al. 2009, Hoang et al. 2011). However, a power-law behaviour is compatible with most detections above 23 GHz (Banday et al. 2003, Davies et al. 2006, Ghosh et al. 2012). This could be the result of a superposition of more peaked components along the line of sight or could indicate a peak frequency lower than 23 GHz. The most recent *WMAP* 9-yr results quote a peak frequency at low latitudes ranging from 10 to 20 GHz for the spectrum in K_{R-J} units, which means 20–30 GHz when considering flux density units.

3.3. Component separation pipeline

Several component separation methods adopt the linear mixture data model (see Appendix A for full derivation). For each line of sight we write:

$$\boldsymbol{x} = \mathsf{H}\boldsymbol{s} + \boldsymbol{n}, \quad (3)$$

where $\boldsymbol{x}$ and $\boldsymbol{n}$ contain the data and the noise signals. They are vectors of dimension $N_{\rm d}$, which is the number of frequency channels considered. The vector $\boldsymbol{s}$, having dimension $N_{\rm c}$, contains the $N_{\rm c}$ unknown astrophysical components (e.g. CMB, dust emission, synchrotron emission, free-free emission, AME) and the $N_{\rm d} \times N_{\rm c}$ matrix H, called the mixing matrix, contains the frequency scaling of the components for all the frequencies. The elements of the mixing matrix are computed by integrating the source emission spectra within the instrumental bandpass. When working in the pixel domain, Eq. (3) holds under the assumption that the instrumental beam is the same for all the frequency channels. In the general case, this is achieved by equalizing the resolution of the data maps to the lowest one. When working in the harmonic or Fourier domain, the convolution for the instrumental beam is a multiplication and is linearized without assuming a common resolution.

Within the linear model, we can obtain an estimate $\hat{\boldsymbol{s}}$ of the components $\boldsymbol{s}$ through a linear mixture of the data:

$$\hat{\boldsymbol{s}} = \mathsf{W}\boldsymbol{x}, \quad (4)$$

where W is called the reconstruction matrix. Suitable reconstruction matrices can be obtained from the mixing matrix H. For example:

$$\mathsf{W} = [\mathsf{H}^T\mathsf{C}_{\rm n}^{-1}\mathsf{H}]^{-1}\mathsf{H}^T\mathsf{C}_{\rm n}^{-1} \quad (5)$$

is called the generalized least square (GLS) solution and only depends on the mixing matrix and on the noise covariance $\mathsf{C}_{\rm n}$.

The mixing matrix is the key ingredient of component separation. However, as discussed in Sec. 3.2, the frequency spectra of the components are not known with sufficient precision to perform an accurate separation. To overcome this problem, our component separation pipeline implements a first step in which

Table 2. Summary of ancillary data.

Central frequency [GHz]	Label	Resolution [arcmin]	Reference
0.408	Haslam	60	Haslam et al. (1982)
	Hα	60	Dickinson et al. (2003)
	Hα	6–60	Finkbeiner (2003)
22.8–94	*WMAP* 7-yr	56.8–13.8	Jarosik et al. (2011)
94		60	Finkbeiner et al. (1999)
2997	100 μm	5	Schlegel et al. (1998)
24983, 2997	IRIS Band 1, 4	4	Miville-Deschênes & Lagache (2006)
	$E(B-V)$	5	Schlegel et al. (1998)

the mixing matrix is estimated from the data and a second one in which this result is exploited to reconstruct the amplitudes of the components.

3.3.1. Estimation of the mixing matrix

For the mixing matrix estimation we rely on the CCA (Bonaldi et al. 2006, Ricciardi et al. 2010), which exploits second-order statistics of the data to estimate the frequency scaling of the components on defined regions of the sky (sky patches). We used the harmonic-domain version of the CCA, whose basic principles of operation are reported in Appendix A. This code works on square sky patches using Fourier transforms. It exploits the data auto- and cross-spectra to estimate a set of parameters describing the frequency scaling of the components. The patch-by-patch estimation prevents the detection of small-scale spatial variations of the spectral properties. On the other hand, by using a large number of samples we retain more information, which provides good constraints, even when the components have similar spectral behaviour. The CCA has been successfully used to separate the synchrotron, free-free and AME components from *WMAP* data in Bonaldi et al. (2007).

We used a patch size of $20^\circ \times 20^\circ$, obtained as a trade-off between having enough statistics for a robust computation of the data cross-spectra and limited spatial variability of the foreground properties. Given the dimension of the region of interest, we have 10 independent sky patches. However, exploiting a redundant number of patches, widely overlapping with each-other, enables us to eradicate the gaps between them and obtain a result that is independent of any specific selection of patches. We covered the region of interest with patches spaced by 2° in both latitude and longitude. By re-projecting the results of the CCA on a sphere and averaging the outputs for each line of sight we can synthesize smooth, spatially varying maps of the spectral parameters (see Ricciardi et al. 2010 for more details).

3.3.2. Reconstruction of the component amplitudes

The reconstruction of the amplitudes has been done in pixel space at 1° resolution using Eq. (5), exploiting the output of the previous step. To equalize the resolution of the data maps, the $a_{\ell m}$ of each map have been multiplied by a window function, $W_S^{(\ell)}$, given by a 1° Gaussian beam divided by the instrumental beam of the corresponding channel (assumed to be Gaussian with full width half maximum (FWHM) as specified in Table 1). This corresponds, in real space, to convolution with a beam B_S. In order to obtain an estimate of the corresponding noise after smoothing, the noise variance maps should be convolved with $B_N = (B_S)^2$. We did this again in harmonic-space, after having obtained the window function $W_N^{(\ell)}$, corresponding to B_N, by Legendre transforming $W_S^{(\ell)}$, squaring the result, and Legendre transforming back.

The smoothing process also correlates noise between different pixels, which means that the RMS per pixel obtained as detailed above is not a complete description of the noise properties. However, the estimation of the full covariance of noise (and its propagation through the separation in Eqs. (4) and (5)) is very computationally demanding. In this work we take into account only the diagonal noise covariance and neglect any correlation between noise in different pixels. In a signal-dominated case, such as the one considered here, the errors on the noise model have very small impact on the results.

4. AME frequency spectrum

We modelled the mixing matrix to account for five components: CMB; synchrotron emission; thermal dust emission; free-free emission; and AME. We neglected the presence of the CO component by excluding from the analysis the 100 and 217 GHz *Planck* channels, which are significantly contaminated by the CO lines $J = 1 \rightarrow 0$ and $J = 2 \rightarrow 1$ respectively (Planck HFI Core Team 2011b). CO is also present at 353 GHz, where it can contaminate the dust emission by up to 3% in the region of interest, and at 545 and 857 GHz, where the contamination is negligible. For the estimation of the mixing matrix we used the following dataset:

- *Planck* 30, 44, 70, 143 and 353 GHz channels;
- *WMAP* 7-yr K band (23 GHz);
- Haslam 408 MHz map;
- Predicted free-free emission at 23 GHz based on the Hα Dickinson et al. (2003) template corrected for dust absorption with the Schlegel et al. (1998) $E(B-V)$ map by assuming a dust absorption fraction of 0.33.

We verified that the inclusion of the *WMAP* Ka–W bands in this analysis did not produce appreciable changes in the results. The explored frequency range is now covered by *Planck* data with higher angular resolution and sensitivity. Caution is needed when using Hα as a free-free tracer: dust absorption (Dickinson et al. 2003) and scattering of Hα photons from dust grains (Wood & Reynolds 1999, Dong & Draine 2011) cause dust-correlated errors in the free-free template, which could bias the AME spectrum. The impact of such biases has been assessed through simulations as described in Sect. 4.1.

For dust emission we used the model of Eq. (1) with $T_d = 18$ K and estimated the dust spectral index β_d. The reason why we fixed the dust temperature is that this parameter is mostly constrained by high-frequency data, which we do not include

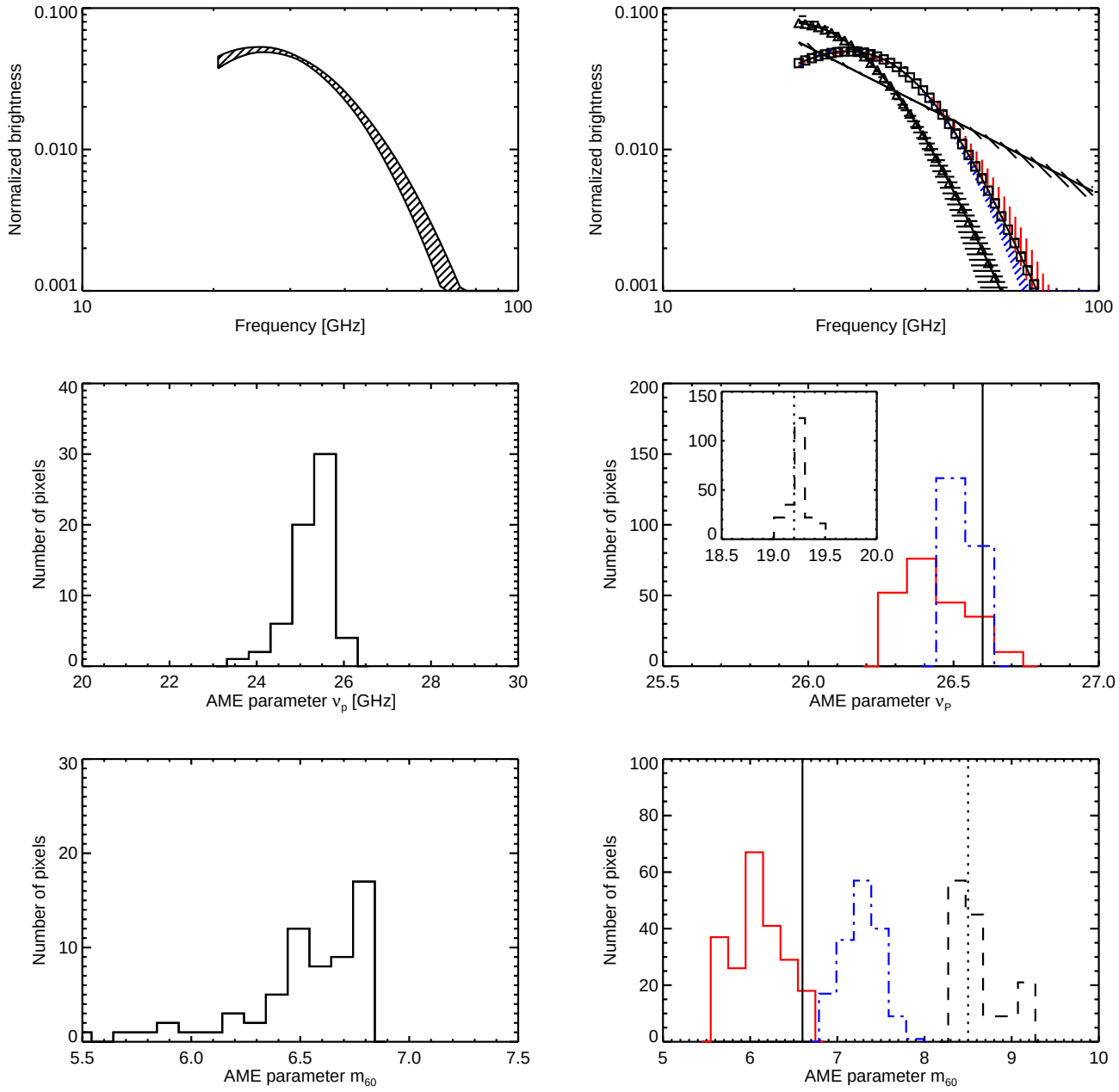

Fig. 3. CCA estimation of the AME frequency spectrum in the region of interest for real data (left panels) and simulated data (right panels). *Top*: areas spanned by the estimated spectra including 1σ errors. *Middle and bottom*: histograms of the spectral parameters m_{60} and $\nu_{\rm p}$ on $N_{\rm side} = 16$ estimated spectral index maps. For the simulated case (right panels) we consider two convex spectra peaking at 19 GHz and 26 GHz and a power-law model. Top right: the true inputs are shown as solid black lines (power-law) with triangles (19 GHz peak) and squares (26 GHz peak) and the estimations as shaded areas. The blue and red colours show estimations done exploiting the free-free templates FF_1 and FF_2 described in Appendix C. Middle and bottom right panels: the true inputs are shown by solid and dotted vertical lines for the simulations peaking at 26 GHz and 19 GHz respectively; the blue dot-dashed and red solid histograms show the estimations carried out using the FF_1 and FF_2 templates, and the black dashed lines show the estimations for the 19 GHz input spectrum.

in this analysis. The temperature $T_{\rm d} = 18$ K is consistent with the 1-component dust model by Finkbeiner et al. (1999) and in good agreement with the median temperature of 17.7 K estimated at $|b| > 10^\circ$ by Planck Collaboration XIX (2011). For the dust spectral index we obtained $\beta_{\rm d} = 1.73 \pm 0.09$. For synchrotron radiation we adopted a power-law model with fixed spectral index $\beta_{\rm s} = -2.9$ (e.g., Miville-Deschênes et al. 2008), as the weakness of the signal prevented a good estimation of this parameter. We verified that different choices for $\beta_{\rm s}$ (up to a 10 % variation, $\beta_{\rm s}$ from -2.6 to -3.2) changed the results for the other parameters only of about 1 %, due to the weakness of the synchrotron component with respect to AME and thermal dust. As a spectral model for AME we adopted the best-fit model of Bonaldi et al. (2007), which is a parabola in the log(S)-log(ν)

plane parametrized in terms of peak frequency ν_p[2] and slope at 60 GHz m_{60}:

$$\log T_{\mathrm{RJ,AME}}(\nu) \propto \left(\frac{m_{60}\log\nu_p}{\log(\nu_p/60)} + 2\right)\log\nu + \frac{m_{60}(\log\nu)^2}{2\log(\nu_p/60)}. \quad (6)$$

Details of the model and justification of this choice are given in Appendix B. We also tested a pure power-law model ($\nu \propto \nu^\alpha$) for AME, fitting for the spectral index α, but we could not obtain valid estimations in this case. This is what we expect when the true spectrum presents some curvature, as verified through simulations (see Sect. 4.1 and Appendix C).

Our results for the AME spectrum are shown in the left panels of Fig. 3. On average, the AME peaks at 25.5 GHz, with a standard deviation of 0.6 GHz, which is within estimation errors (1.5 GHz). This means we find no significant spatial variations of the spectrum of the AME in the region of the sky considered here. However, we recall that this only applies to diffuse AME, as our pipeline cannot detect small-scale spatial variations, and we are restricted to a limited area of the sky.

Our results on the peak frequency of the AME are similar to those of Planck Collaboration XX (2011) for Perseus and ρ Ophiuchi and (Planck Collaboration TBC 2013) on compact dust clouds. *WMAP* 9-yr MEM analysis (Bennett et al. 2012) measures the position of the peak for the spectrum in K_{R-J} units and finds a typical value of 14.4 GHz for diffuse AME at low latitudes, which roughly corresponds to 27 GHz when the spectrum is in flux density units. According to previous work, at higher latitudes the peak frequency is probably lower (see e.g. Banday et al. 2003, Davies et al. 2006, Ghosh et al. 2012). Interestingly, the same CCA method used in this paper yields ν_p around 22 GHz when applyied to the North Celestial Pole region (towards $l = 125°$, $b = 25°$, Bonaldi & Ricciardi 2012). Spatial variations of the AME spectrum could explain these differences.

4.1. Assessment through simulations

The reliability of our results has been tested with simulations. The main purposes of this assessment are:

- to verify the ability of our procedure to accurately recover the AME spectrum for different input models;
- to investigate how the use of foreground templates — free-free in particular — can bias the results.

We did this by applying the procedure described in Sect. 4 to sets of simulated data, for which the true inputs are known. For the first target, we performed three separate simulations including a different AME model: two spinning dust models, peaking at 19 GHz and 26 GHz, and a spatially varying power-law. For the second target, we introduced dust-correlated biases in the free-free template and quantified their impact on the estimated parameters. The full description of the simulations and of the tests performed is given in Appendix C.

The results are displayed in the right panels of Fig. 3. In the top panel we show, for each of the three tested input models, the true spectrum (solid line) and the estimated spectrum with errors (shaded area). The red and blue areas distinguish between two free-free templates (referred to as FF_1 and FF_2), which are biased in a different way with respect to the simulated free-free component. In the middle and bottom panels we show the histograms of the recovered spectral parameters compared with the true inputs (vertical lines); the red and blue colours are as before. We conclude the following:

- If the input AME is a convex spectrum, we are able to accurately recover the peak frequency, ν_p, for both the 19 and 26 GHz input values. Our pipeline is able to distinguish very clearly between the two input models; biases in the free-free template do not affect the recovery of the peak frequency.
- The estimated spectrum can be slightly biased above 40–50 GHz, where the AME is faint, as a result of limitations of the spectral mode we are using (see Appendix B) and errors in the free-free template. The systematic error on m_{60} is quantified as 0.5–0.6.
- If the input AME spectrum is a power-law, we obtain a good recovery when fitting for a spectral index.

When the AME is a power-law the parabolic model is clearly wrong, as the parameter describing the position of the peak is completely unconstrained and the model steepens considerably with frequency. Similarly, when the AME is a curved spectrum the power-law model is too inaccurate to describe it. As expected, both these estimations fail to converge.

5. Reconstruction of the amplitudes

The reconstruction of the amplitude of the components has been performed on the 1° resolution version of the dataset. We used the same frequencies exploited for the estimation of the mixing matrix, except for the free-free template, which has been excluded to avoid possible biases in the reconstruction. The results are shown in Fig. 4. The first and second rows show the components reconstructed at 30 GHz (from left to right: synchrotron emission, free-free emission, AME, and thermal dust emission) and the corresponding noise RMS maps. Thanks to the linearity of the problem, the noise variance maps can be obtained by combining the noise variance maps of the channels at 1° degree resolution with the squared reconstruction matrix W. The noise on the synchrotron and thermal dust maps is low compared to that for free-free and AME. This is because the 408 MHz map and the *Planck* 353 GHz channel give good constraints on the amplitudes of synchrotron and thermal dust emission respectively.

The AME component is correlated at about 60 % and 70 % with the 100 μm and the $E(B-V)$ dust templates by Schlegel et al. (1998), 40 % with Haslam et al. (1982) 408 MHz and 20 % with Hα. This favours emission mechanisms based on dust rather than to other hypotheses, such as curved synchrotron emission and free-free emission. The $E(B-V)$ template correlates better with thermal dust emission than the 100 μm map (the correlation coefficients being 0.73 ± 0.01 and 0.96 ± 0.01 respectively). This is expected if AME is dust emission. In fact, both spinning dust and thermal dust emission are proportional to the column density, for which $E(B-V)$ is a better estimator than the 100 μm emission, which is strongly affected by the dust temperature.

The errors due to the separation process (third and fourth row of Fig. 4) are obtained by propagating via Monte-Carlo the uncertainties on the mixing matrix estimated by CCA to the reconstruction of the components (see Ricciardi et al. 2010 for more details). Essentially, the mixing matrix parameters are randomized according to their posterior distributions; the component separation error on the amplitudes is estimated as the variance of GLS reconstructions for different input mixing matrices.

One complication is that in the present analysis we did not estimate the synchrotron spectral index, but we fixed it at $\beta_s = -2.9$. Thus, we do not have errors on the synchrotron spectral index from our analysis. We therefore considered two cases:

[2] The peak frequency ν_p is defined for the specrum in flux density units

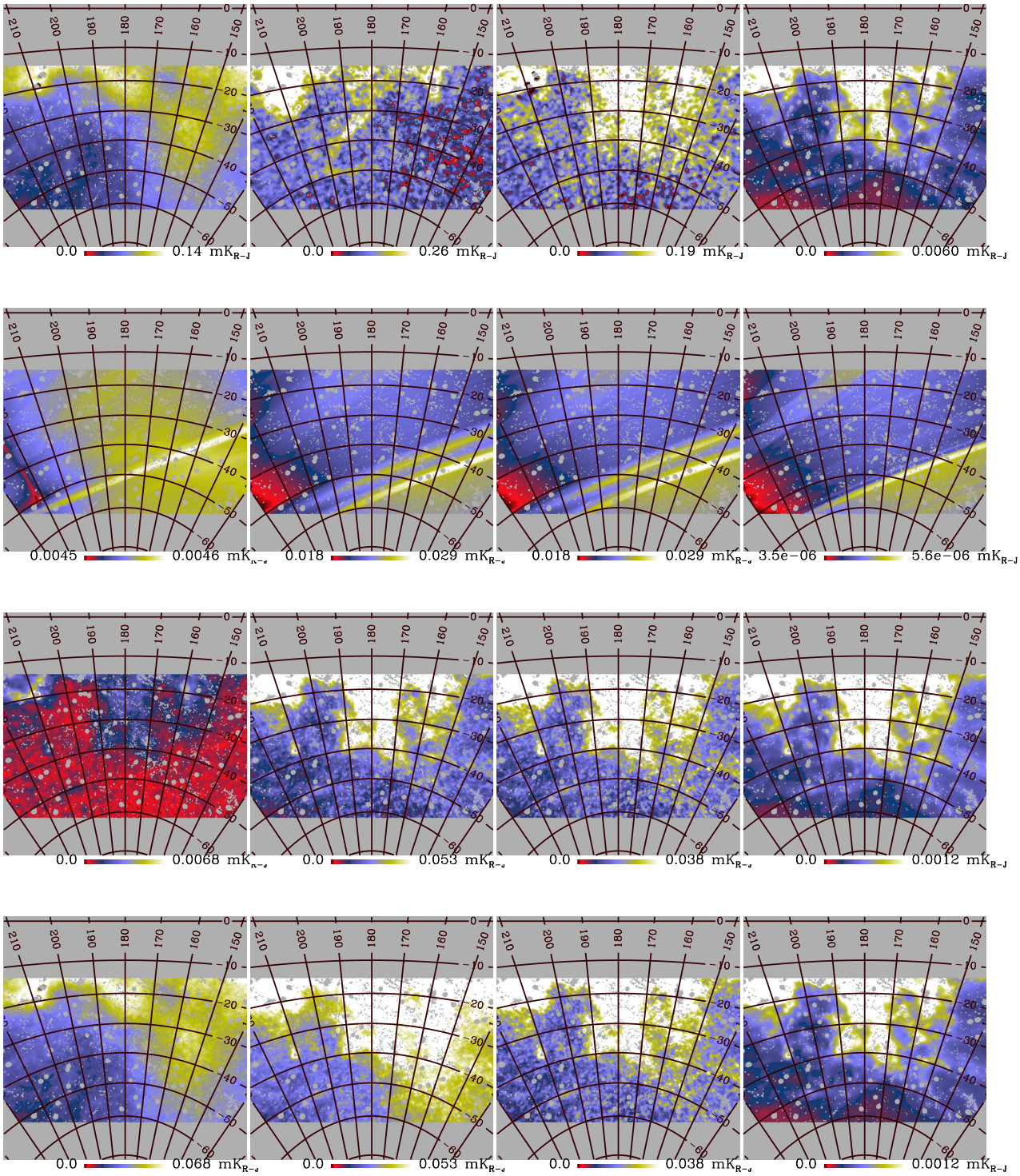

Fig. 4. 1° resolution reconstruction at 30 GHz of (from left to right): synchrotron emission; free-free emission; AME; and thermal dust emission. These reconstructions are performed as described in Sect. 3.3.2. Rows from top to bottom: component amplitudes; noise RMS; predicted RMS of component separation error due to the estimation of AME and thermal dust spectra; and predicted RMS of component separation error including a random error on $\beta_s = -2.9 \pm 0.1$.

one in which we propagated only the errors on the AME and thermal dust spectral parameters, thus assuming no error on β_s (third row of Fig. 4); and another in which we included an indicative random error $\Delta\beta_s = 0.1$ (last row of Fig. 4).

The predicted error due to separation is generally higher than noise and on average of the order 15–20 % of the component amplitude for AME, free-free, and dust. Once we allow some scatter on β_s, the predicted error on synchrotron emission becomes of the order of 50 %: this indicates that the reconstruction of this

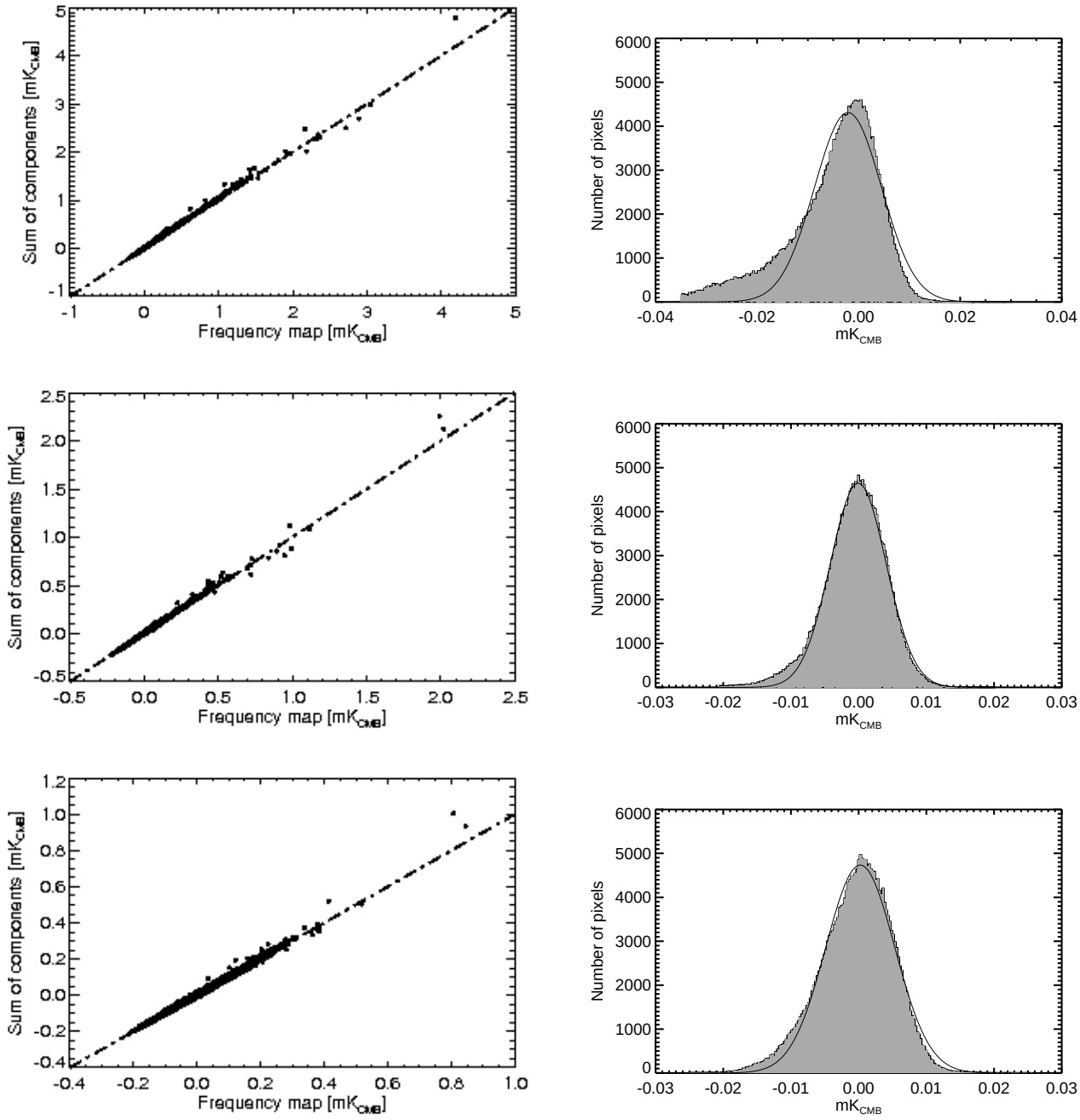

Fig. 5. *Left panels*: sum of the components vs frequency maps at (from top to bottom) 30, 44, and 70 GHz. The line is the $x = y$ relation. *Right panels*: pixel distribution of the residual (frequency map-sum of the components) maps compared to the best-fit Gaussian distribution.

component is essentially prior-driven. The inclusion of $\Delta\beta_s$ has some effect on the error prediction for free-free emission, while AME and dust are mostly unaffected.

To evaluate the quality of the separation we compared the frequency maps with the sum of the reconstructed components at the same frequency. In the left panels of Fig. 5 we plot the sum of the components for 30, 44, and 70 GHz against the amplitude of the frequency map. The comparison is made at 1° resolution with $N_{side} = 128$ pixels. The dashed line indicates the $x = y$ relation, which corresponds to the ideal case in which the two maps are identical.

The agreement between data and predictions is in general very good. The scatter of the points does not measure the quality of the separation but the signal-to-noise of the maps. It increases from 30 to 70 GHz, as the foreground signal gets weaker. The errors in the component separation show up as systematic departures of the data from the prediction. As those are not apparent, we also show on the right panels of Fig. 5 the pixel distribution of the residual map compared to the best-fit Gaussian distribution. At 44 and 70 GHz the scatter, though quite small, dominates the residual and covers the systematic effects, with the exception of a few outliers, mostly due to compact sources. At 30 GHz the scatter is low enough to reveal a feature: a sub-sample of pixels

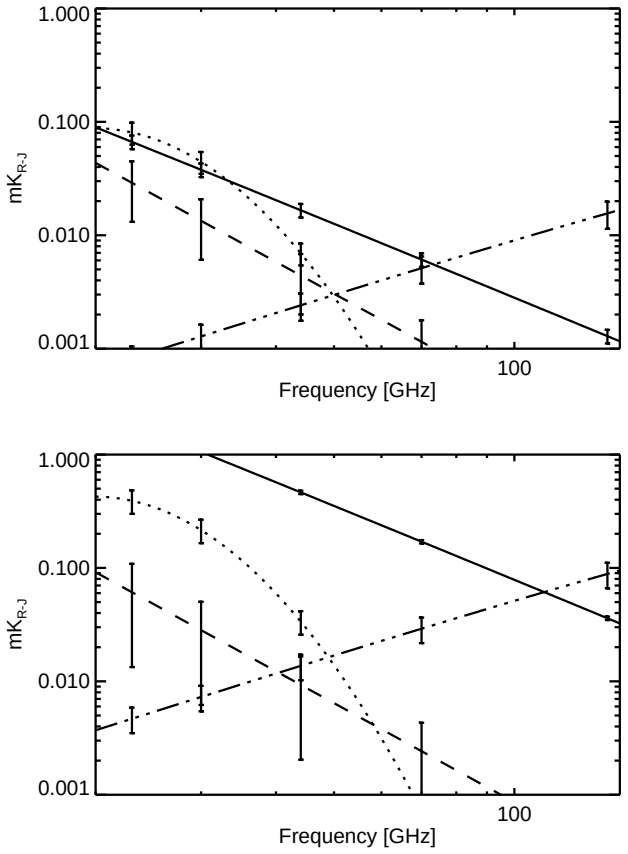

Fig. 6. Estimated spectra of synchrotron emission (dashed line), free-free emission (solid line), thermal dust emission (dash-dotted line) and AME (dotted line) for average local properties (top) and for Barnard's region (bottom).

in which the reconstructed signal is higher than the true one, thus creating a negative in the residual.

This kind of systematic effect is very difficult to avoid when separating many bright components, because small errors in the mixing matrix cause bright features in the residual maps. Our Monte-Carlo approach is however able to propagate these errors. At 30 GHz the brightest components are AME and free-free emission, for which the predicted component separation error is on average 0.04–0.05 $\mathrm{mK_{CMB}}$, in agreement with the level of the non-Gaussian residuals. Coherent structures in the residual maps are induced by the low resolution of the maps of spectral parameters, which means that over nearby pixels the error in the mixing matrix, and thus on the separation, is similar.

In Fig. 6 we show the amplitude of the components as a function of frequency. The top panel represents the typical behaviour in the Gould Belt, while the bottom one refers to a particular case, Barnard's region where free-free emission is particularly strong. The points are the average amplitude of the components at each frequency within the selected regions of the sky. The scaling of the amplitudes with frequency is, by construction, given by the spectral model estimated with CCA. The error bars measure the scatter induced on the amplitudes by the errors on the spectral parameters (also including $\Delta\beta_\mathrm{s} = 0.1$).

6. Free-free electron temperature

The intensity of the free-free emission at a given frequency with respect to Hα can be expressed as

$$\frac{T_\mathrm{ff}(\nu)[\mu\mathrm{K_{R-J}}]}{\mathrm{H}\alpha[\mathrm{Rayleighs}]} = 14\,T_4^{0.517} \times 10^{0.029/T_4} \times 1.08\,G(\nu)(\nu/10)^{-2}, \quad (7)$$

where G(ν) is the Gaunt factor already introduced in Sect. 3.2 and T_4 is the electron temperature T_e in units of 10^4 K. One caveat is that dust absorbs Hα emission; this can be quantified by the dust absorption fraction f_d (Dickinson et al. 2003). Therefore f_d and T_e are degenerate parameters.

The ratio $T_\mathrm{ff}(\nu)/\mathrm{H}\alpha$ can be obtained by comparing the Hα and free-free emission from component separation through a temperature-temperature plot (TT analysis). We made free-free versus Hα plots by using the CCA free-free solution at 30 GHz and both Dickinson et al. (2003) and Finkbeiner (2003) Hα templates corrected for dust absorption for different values of f_d. We considered 3° resolution maps, sampled with $N_\mathrm{side} = 64$ pixels. Besides point sources, we excluded from the analysis the region most affected by dust absorption based on the Schlegel et al. (1998) $E(B-V)$ map, as shown in the left panel of Fig. 7. The electron temperature T_e has been inferred by fitting the data points with a linear relation and converting the best-fit slope to T_e through Eq. (7). The error on T_e has been derived from the error on the best-fit slope given by the fitting procedure, through error propagation. In the right panel of Fig. 7 we show the TT plots for the Dickinson et al. (2003) Hα template, with different colours corresponding to different values of f_d, and the best-fit linear relations. The electron temperatures are reported in the top part of Table 3. We obtain $T_\mathrm{e} = 6000$–3500 K with $f_\mathrm{d} = 0$–0.5 for the Dickinson template; the Finkbeiner template yields higher, but consistent, values ($T_\mathrm{e} = 7000$–4500 K with $f_\mathrm{d} = 0$–0.5).

6.1. Comparison with cross-correlation with templates

An alternative way to compute $T_\mathrm{ff}(\nu)/\mathrm{H}\alpha$ and T_e is through cross-correlation of the Hα template with frequency maps (CC analysis). We cross-correlate simultaneously the templates for free-free, dust, and synchrotron emission, as described in Ghosh et al. (2012). We used the 408 MHz map from Haslam et al. (1982) as a tracer of synchrotron emission, Dickinson et al. (2003) Hα as a tracer of free-free emission and the Finkbeiner et al. (1999) model eight 94 GHz prediction as a tracer of dust emission. We used the same resolution, pixel size and sky mask adopted for the TT analysis (3° and $N_\mathrm{side} = 64$). As pointed out by Ghosh et al. (2012), at this resolution the template-fitting analysis is more reliable than at 1° because the smoothing reduces artifacts in the templates. The correlation coefficients are computed for each emission process at a given frequency by minimizing the generalized χ^2 expression. We also fitted for an additional monopole term that can account for offset contributions in all templates and the data in a way that does not bias the results (Macellari et al. 2011). The chance correlation of the templates with the CMB component in the data causes a systematic error in the correlated coefficients and has been estimated using simulations. We generated 1000 random realizations of the CMB using the best-fit ΛCDM model [3] and cross-correlated each of them using the templates with the same procedure applied to the data. The amplitude of the predicted chance correlation, given by the RMS over the 1000 realizations, is $1.13\,\mu\mathrm{K_{CMB}}/\mu\mathrm{K_{CMB}}$

[3] http://lambda.gsfc.nasa.gov/product/map/dr4/pow_tt_spec_get.cfm

Table 3. Inferred T_e [K] for TT analysis and CC analysis using different Hα templates and dust absorption fractions f_d.

Method	Template	$f_d = 0.0$	$f_d = 0.1$	$f_d = 0.3$	$f_d = 0.5$
TT analysis	Dickinson	5900 ± 2500	5500 ± 2500	4700 ± 2200	3500 ± 1600
	Finkbeiner	6800 ± 2500	6400 ± 2500	5500 ± 2400	4600 ± 1900
CC analysis	Dickinson	4900 ± 1100	4000 ± 1000	2600 ± 850	2000 ± 700
	Finkbeiner	7000 ± 1300	6400 ± 1200	5000 ± 1000	3400 ± 840

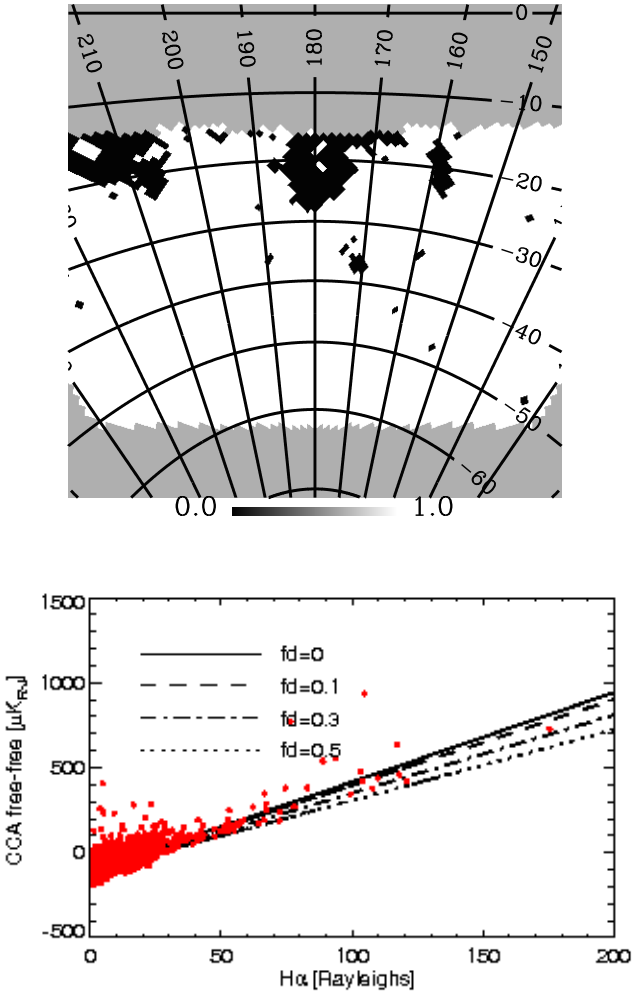

Fig. 7. TT analysis for estimation of T_e. *Top*: gnomonic projection showing the mask used (masked pixels are in black, while pixels used in the analysis are in white). *Bottom*: TT plot comparing the CCA free-free solution with the Hα template for $f_d = 0$ (points) and linear fits to the TT plots for different values of f_d (lines).

for the dust template, 1.12 μK_{CMB}/R for the free-free template and 3.8 μK_{CMB}/K for the synchrotron template.

In the top panel of Fig. 8 we compare the Hα correlation coefficients (points with error bars) with the component separation results for free-free emission obtained in Sect. 5 (shaded area). The flux for both the component separation and cross-correlation has been computed as the standard deviation of the maps (the separated free-free map and the scaled Hα template, respectively) as this is not affected by possible offsets between the *Planck* data and the Hα template. There is generally good agreement between the two results; in the frequency range 40–60 GHz there is an excess in the correlated coefficients, which could be indicative of a contribution from the AME component (similar to that found by Dobler & Finkbeiner 2008b). Flattening of the CC coefficients for $\nu > 60$ GHz is consistent with positive chance correlation between the CMB and the Hα template.

The dust-correlated coefficients are compared with the component separation results in the bottom panel of Fig. 8. The agreement is very good for $\nu < 40$ GHz and $\nu > 100$ GHz, where AME and thermal dust emission are strong. In the 40–70 GHz range the CC results are higher than the component separation results. As discussed in Appendix B, the parametric fit to the AME spectrum implemented by CCA could be inaccurate in this frequency range, where the AME is faint. Alternatively, a similar effect could be explained by the presence of a secondary AME peak, around 40 GHz (e.g. Planck Collaboration XX 2011, Ghosh et al. 2012) or flattening of the dust spectral index towards low frequencies, which are not included in our spectral model. Discriminating between these hypotheses is not possible given the large error bars.

To determine the free-free electron temperature the Hα correlation coefficients have been fitted with a combination of power-law free-free radiation (with fixed spectral index of −2.14) and a CMB chance correlation term (which is constant in thermodynamic units). The amplitude of the free-free component with respect to Hα resulting from the fit, and its uncertainty, yield T_e and the corresponding error bar. The results for the Gould Belt region outside the adopted sky mask are reported in the bottom part of Table 3. We find T_e = 5000–2000 K for f_d = 0–0.5 with the Dickinson et al. (2003) template, and T_e = 7000–3500 K for f_d = 0–0.5 with the Finkbeiner (2003) template.

With respect to the TT analysis, these results are more sensitive to the choice of the template and the f_d correction. In fact, the correlation coefficients mostly depend on the brightest features in the map, which can differ significantly from one template to another, while the fit of the TT plot is driven by the larger sample of pixels, which is more difficult to modify in a systematic way. The CC results are always consistent with the TT ones; however, we note that, for the Dickinson template, they are systematically lower. One possible explanation is that the two methods have different sensitivity to errors in the template or in the model used. Spatial variability of T_e could also give a systematic difference in the results, since the two approaches weight pixels differently. This confirms that estimating the free-free electron temperature is a difficult problem and that caution is needed when interpreting the results.

7. AME as spinning dust emission.

An explanation that is often invoked for the AME is electric dipole radiation from small, rapidly spinning, Polycyclic Aromatic Hydrocarbon (PAHs) dust grains (Erickson 1957,

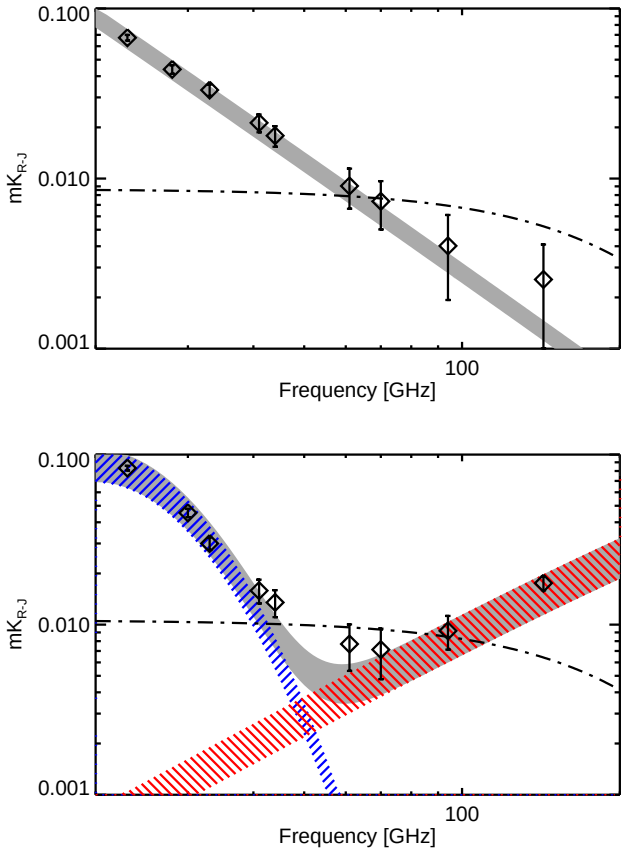

Fig. 8. Comparison between correlation coefficients (symbols with error bars) and component separation results (shaded areas) for free-free emission (top) and dust emission (bottom). For free-free emission we show the Dickinson et al. (2003) Hα correlation coefficients and for dust emission the Finkbeiner et al. (1999) correlation coefficients. The grey area in the bottom panel is the sum of the AME (blue) and thermal dust (red) components. The dash-dotted line in both panels shows the 1σ error due to the chance correlation of CMB with foreground templates, estimated using simulations.

Draine & Lazarian 1998, Dobler & Finkbeiner 2008b, Dobler et al. 2009, Hoang et al. 2011).

Alternatively, the AME could be due to synchrotron radiation with a flat (hard) spectral index (e.g. Bennett et al. 2003). The presence of such a hard spectrum synchrotron component could be highlighted by comparing the 408 MHz map of Haslam et al. (1982), which would predominantly trace steep spectrum radiation, with the 2.3 GHz map by Jonas et al. (1998), which would be more sensitive to flat spectrum radiation. This issue has been studied in detail by Peel et al. (2011) using a cross-correlation of *WMAP* 7-yr data with foreground templates. They analysed the region defined by $170^\circ \leq l \leq 210^\circ$, $-55^\circ \leq b \leq -25^\circ$ and found that the dust-correlated coefficients are mostly unaffected by the use of the 2.3 GHz template instead of the 408 MHz template. This indicates that hard synchrotron radiation cannot account for most of the dust-correlated component at low frequencies.

To check the hypothesis of spinning dust emission we applied the method proposed by Ysard et al. (2011), which exploits the `SpDust` (Ali-Haïmoud et al. 2009, Silsbee et al. 2011) and `DustEM` (Compiègne et al. 2011) codes, to model the frequency spectra of thermal and anomalous dust emission from the microwaves to the IR. The dust populations and properties are assumed to be the same as in the diffuse interstellar medium at high Galactic latitude (DHGL), defined in Compiègne et al. (2010). This model includes three dust populations: PAHs; amorphous carbonaceous grains; and amorphous silicates. For PAHs, it assumes a log-normal size distribution with centroid $a_0 = 0.64$ nm and width $\sigma = 0.4$, with a dust-to-gas mass ratio $M_{\rm PAH}/M_{\rm H} = 7.8 \times 10^{-4}$.

By fitting the thermal dust spectrum with `DustEM` we determine the local intensity of the interstellar radiation field, G_0 (the scaling factor with respect to a UV flux of 1.6×10^{-3} erg s^{-1}cm^{-2} integrated between 6 and 13.6 eV), and the hydrogen column density, $N_{\rm H}$. We then fit the AME spectrum with `SpDust`, the only free parameter being the local hydrogen density $n_{\rm H}$. We assume a cosmic-ray ionization rate $\zeta_{\rm CR} = 5 \times 10^{-17}$ s^{-1}H^{-1}, and take the electric dipole moment to be as in Draine & Lazarian (1998), a prescription also shown to be compatible with the AME extracted from *WMAP* data (Ysard et al. 2010). It is worth noticing that there is a degeneracy with the size of the grains (smaller size yields higher peak frequency and intensity of the AME). However, the size distribution can only be constrained using shorter wavelength data (typically 3–8 μm). The size we are adopting (0.64 nm) is motivated by its ability to reproduce the data in the mid-IR (Compiègne et al. 2011); other models adopt different sizes (e.g. 0.54 nm and 0.5 nm in Draine & Li 2001 and Draine & Li 2007 respectively).

As the Gould Belt region contains strong foreground emission components, significantly correlated with each-other, we expect different environments to be mixed in a complex way. In order to obtain meaningful results for the physical modelling we tried to isolate sub-regions where single environments dominate. To first order, we can use the free-free emission as a tracer of the ionized gas environment, CO emission as a tracer of molecular gas, and associate the rest of the emission with the diffuse ISM. In Fig. 9 we schematically map the different environments by setting a threshold on the free-free emission coming from component separation, the CO emission from *Planck*, and the total foreground emission at 30 GHz. We identified two relatively big sub-regions (shown as circles in Fig. 9) as selections which are dominated by ionized gas and diffuse ISM environments. It would not be meaningful to consider smaller areas because of the patch-by-patch estimation of the AME frequency scalings, which means that our AME spectra are averaged over relatively large areas of the sky. Due to the clumpiness of the molecular gas environment it was not possible to select a region for this case. It is worth noting that some molecular gas may be contained in the diffuse ISM region.

The spectra of AME and thermal dust in the 20–353 GHz frequency range are based on component separation results. The frequency scaling is that estimated with CCA and the normalization is given by the average of the reconstructed amplitude map in the region of the sky considered. The error bars on the data points include the RMS of the amplitude in the same region (considered as the error in the normalization) and the errors on the estimated spectral parameters. The thermal dust spectra have been complemented with higher frequency data points computed directly from the frequency maps: *Planck* 545 GHz and 857 GHz; IRIS 100 μm map; and the IRIS 12 μm map corrected for Zodiacal light emission used in Ysard et al. (2010).

The results of the modelling for the ionized gas and diffuse ISM regions within the Gould Belt are shown in Fig. 10. The empirical spectra of AME coming from component separation can be successfully modelled as spinning dust emission for both regions. The match between data and model becomes worse at

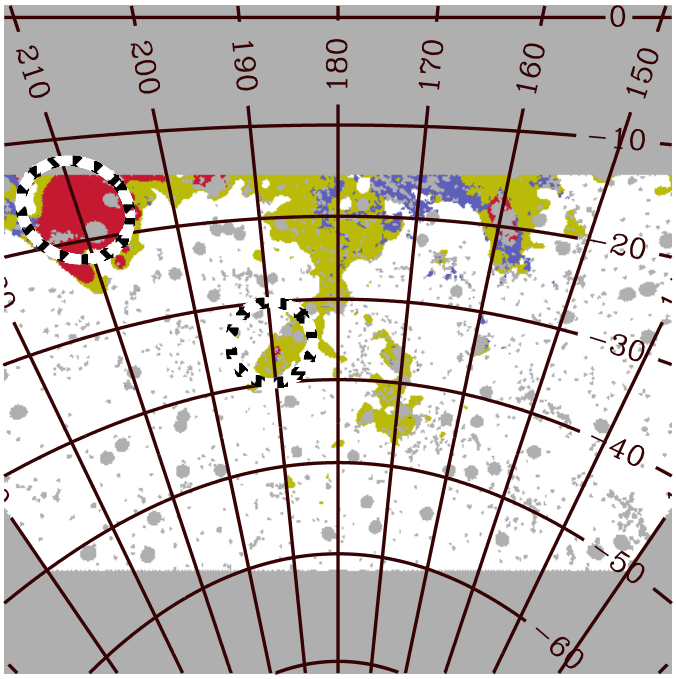

Fig. 9. Partitioning of the Gould Belt region based on thresholds over free-free emission (red), CO emission (blue), and total emission at 30 GHz (yellow), used as tracers of H II gas, molecular gas, and diffuse ISM environments, respectively, and the rest of the Gould Belt region (light blue). Circled regions are those selected for the computation of spectra and have been labelled as H II-gas (Barnard's arc) and diffuse ISM (centred on $l = 190°$, $b = -35°$) regions, respectively.

higher frequencies, where the AME spectrum could be biased (see Sect. C and Appendix B).

The joint fit of thermal and spinning dust models yields plausible physical descriptions of the two environments. In the top panel of Fig. 10 the diffuse ISM region is modelled with $N_{\rm H} = 2.46 \times 10^{21}$ H cm^{-2}, $G_0 = 0.55$ and $n_{\rm H}$=50 cm^{-3}. The ionized region (middle panel) is modelled with $N_{\rm H} = 5.73 \times 10^{21}$ H cm^{-2}, $G_0 = 0.90$ and $n_{\rm H}$ =25 cm^{-3}.

We tested the stability of these results against calibration errors on the high frequency *Planck* (545 and 857 GHz) and IRIS (100 μm and 12 μm) data (the remaining data points come from the component separation procedure and their error bars already include systematic uncertainties). The actual calibration uncertainty on the *Planck* 545 and 857 GHz channels is estimated to be about 5 %, but is currently being re-evaluated; that on the IRIS data is of the order 10% or larger, especially at 12 μm where it also includes errors on the zodiacal light subtraction. We have verified that very conservative uncertainties up to 20 % both on *Planck* and IRIS data have negligible impact on G_0, while they may affect $N_{\rm H}$ and $n_{\rm H}$ (up to a level of about 10 %). The overall picture however does not change: the ionized region is less dense and illuminated by a stronger radiation field than the diffuse region (which is expected to contain mostly neutral gas). Both the spectra can be modelled as spinning dust emission arising from regions with densities characteristics of the cold neutral medium (CNM, a few tens of H per cm^3). This confirms the results of Planck Collaboration XX (2011) and Planck Collaboration XXI (2011), showing that most of the observed AME could be explained by spinning dust in dense gas. In fact, whenever we have a mixture of warm neutral medium (WNM), warm ionized medium (WIM) and CNM, the spinning dust spectrum is dominated by the denser phase, which emits more strongly. In the bottom panel of Fig. 10 we consider for the ionized region a mixture of two phases, one having lower density ($n_{\rm H} = 0.1$ cm^{-3}, 46 %) and one having higher density ($n_{\rm H} = 55$ cm^{-3}, 54 %), illuminated by the same G_0 as in the middle panel. Such a mixture fits the data somewhat better at 23 GHz than the one-phase model considered previously (the error in the fit at this frequency being 0.3 σ instead of 0.9 σ). In order to fully isolate and study different ISM phases (ionized/neutral, dense/diffuse), both the observations and the analysis should be carried out at high angular resolution.

8. Conclusions

We performed an analysis of the diffuse low-frequency Galactic foregrounds as seen by *Planck* in the Southern part ($130° \le l \le 230°$ and $-50° \le b \le -10°$) of the Gould Belt system, a local star-forming region emitting bright diffuse foreground emission. Besides *Planck* data our analysis includes *WMAP* 7-yr data and foreground ancillary data as specified in Table 2.

We used the CCA (Bonaldi et al. 2006, Ricciardi et al. 2010) component separation method to disentangle the diffuse Galactic foregrounds. In the region of interest the synchrotron component is smooth and faint, and ultimately not well constrained.

The free-free emission is strong and it clearly dominates in the Orion-Barnard region. We inferred the free-free electron temperature both by cross-correlation (CC) of channel maps with foreground templates and temperature-temperature (TT) plots comparing the reconstructed free-free emissio with Hα maps. We obtained $T_{\rm e}$ ranging from 7000 to 2000 K for $f_{\rm d}$=0–0.5, in agreement with other recent results (Ghosh et al. 2012). The use of the Finkbeiner (2003) Hα template yields systematically higher $T_{\rm e}$ than the Dickinson et al. (2003) one. In the case of the TT analysis the difference is around 1000 K ($< 1\sigma$), while for the CC analysis it can reach 2500 K (about 2 σ). The CC results for the Dickinson et al. template are also systematically lower than the TT ones, yet consistent within 1σ.

The AME is the dominant foreground emission at low frequencies over most of the region considered. We estimated the AME peak frequency in flux density units to be 25.5 ± 1.5 GHz, almost uniformly over the region of interest. This is in agreement with AME spectra measured in compact dust clouds (e.g. Planck Collaboration XX 2011) and *WMAP* 9-yr results at low latitudes (once the same convention is adopted, e.g. their AME spectrum is converted from K_{R-J} to flux density, Bennett et al. 2012). In the case of diffuse AME at higher latitudes a lower peak frequency is favoured (Banday et al. 2003, Davies et al. 2006, Ghosh et al. 2012, Bonaldi & Ricciardi 2012). The ability of our pipeline to correctly recover the peak frequency of the AME, $\nu_{\rm p}$, has been verified through realistic simulations. We also considered the effect of systematic errors in the spectral model and in the free-free template and we demonstrated that they have negligible impact on $\nu_{\rm p}$.

Following Peel et al. (2011), a hard (flat spectrum) synchrotron component would not be sufficient to account for the dust-correlated low-frequency emission in this region. In support of the spinning dust mechanism, we performed a joint modelling of vibrational and rotational emission from dust grains as

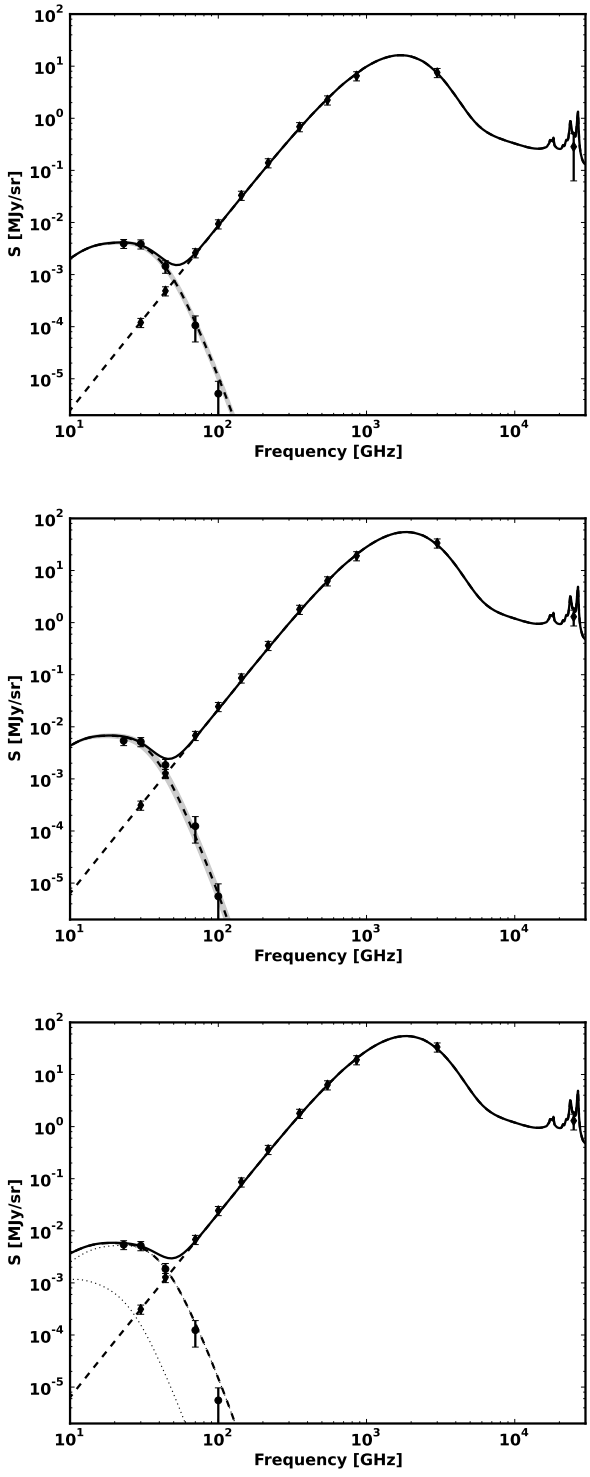

Fig. 10. Frequency spectra (black points with error bars) for thermal dust emission and AME compared, respectively, with `DustEM` and `SpDust` (dashed lines) for the diffuse ISM (top) and ionized gas (middle and bottom) regions within the Gould Belt. The solid line is the sum of the `DustEM` and `SpDust` models. The grey area on the top and middle panels correspond to the $\pm 1\,\sigma$ variations on the best-fit $n_{\rm H}$ values, when fitting for a single phase. In the bottom panel we consider a mixture of two phases ($n_{\rm H} = 0.1\,{\rm cm}^{-3}$ and $n_{\rm H} = 55\,{\rm cm}^{-3}$, in the proportion of 46 % and 54 %, respectively), which marginally improves the fit for the ionized gas region at 23 GHz (the error is $0.3\,\sigma$ instead of $0.9\,\sigma$).

described by Ysard et al. (2011) and we obtained a good description of the data from microwaves to the IR. The fit, which we performed separately for the ionized area near to Barnard's arc and the diffuse emission towards the centre of our region, yields in both cases plausible values for the local density and radiation field. This indicates that the spinning dust mechanism can reasonably explain the AME in the Gould Belt.

9. Acknowledgements

Based on observations obtained with *Planck* (`http://www.esa.int/Planck`), an ESA science mission with instruments and contributions directly funded by ESA Member States, NASA, and Canada.

The development of Planck has been supported by: ESA; CNES and CNRS/INSU-IN2P3-INP (France); ASI, CNR, and INAF (Italy); NASA and DoE (USA); STFC and UKSA (UK); CSIC, MICINN, JA and RES (Spain); Tekes, AoF and CSC (Finland); DLR and MPG (Germany); CSA (Canada); DTU Space (Denmark); SER/SSO (Switzerland); RCN (Norway); SFI (Ireland); FCT/MCTES (Portugal); and The development of Planck has been supported by: ESA; CNES and CNRS/INSU-IN2P3-INP (France); ASI, CNR, and INAF (Italy); NASA and DoE (USA); STFC and UKSA (UK); CSIC, MICINN and JA (Spain); Tekes, AoF and CSC (Finland); DLR and MPG (Germany); CSA (Canada); DTU Space (Denmark); SER/SSO (Switzerland); RCN (Norway); SFI (Ireland); FCT/MCTES (Portugal); and PRACE (EU).

A description of the Planck Collaboration and a list of its members, including the technical or scientific activities in which they have been involved, can be found at `http://www.sciops.esa.int/index.php ?project=planck&page=Planck_Collaboration`. We acknowledge the use of the HEALPix (Górski et al. 2005) package and of the LAMBDA website `http://lambda.gsfc.nasa.gov`.

References

Ali-Haïmoud, Y., Hirata, C. M., & Dickinson, C. 2009, MNRAS, 395, 1055
Alves, M. I. R., Davies, R. D., Dickinson, C., et al. 2012, MNRAS, 422, 2429
Banday, A. J., Dickinson, C., Davies, R. D., Davis, R. J., & Górski, K. M. 2003, MNRAS, 345, 897
Bedini, L. & Salerno, E. 2007, Lecture Notes in Artificial Intelligence, 4964, 9
Bennett, C. L., Halpern, M., Hinshaw, G., et al. 2003, ApJS, 148, 1
Bennett, C. L., Larson, D., Weiland, J. L., et al. 2012, ArXiv e-prints
Bersanelli, M., Mandolesi, N., Butler, R. C., et al. 2010, A&A, 520, A4
Bonaldi, A., Bedini, L., Salerno, E., Baccigalupi, C., & de Zotti, G. 2006, MNRAS, 373, 271
Bonaldi, A. & Ricciardi, S. 2012, Advances in Astronomy, 2012
Bonaldi, A., Ricciardi, S., Leach, S., et al. 2007, MNRAS, 382, 1791
Bond, J. R. & Efstathiou, G. 1987, MNRAS, 226, 655
Boumis, P., Dickinson, C., Meaburn, J., et al. 2001, MNRAS, 320, 61
Broadbent, A., Osborne, J. L., & Haslam, C. G. T. 1989, MNRAS, 237, 381
Compiègne, M., Flagey, N., Noriega-Crespo, A., et al. 2010, ApJ, 724, L44
Compiègne, M., Verstraete, L., Jones, A., et al. 2011, A&A, 525, A103
Davies, R. D. 1960, MNRAS, 120, 483
Davies, R. D., Dickinson, C., Banday, A. J., et al. 2006, MNRAS, 370, 1125
de Oliveira-Costa, A., Tegmark, M., Davies, R. D., et al. 2004, ApJ, 606, L89
Dickinson, C., Davies, R. D., & Davis, R. J. 2003, MNRAS, 341, 369
Dobler, G., Draine, B., & Finkbeiner, D. P. 2009, ApJ, 699, 1374
Dobler, G. & Finkbeiner, D. P. 2008a, ApJ, 680, 1222
Dobler, G. & Finkbeiner, D. P. 2008b, ApJ, 680, 1235
Dong, R. & Draine, B. T. 2011, ApJ, 727, 35
Draine, B. T. & Lazarian, A. 1998, ApJ, 508, 157
Draine, B. T. & Li, A. 2001, ApJ, 551, 807
Draine, B. T. & Li, A. 2007, ApJ, 657, 810
Erickson, W. C. 1957, ApJ, 126, 480
Finkbeiner, D. P. 2003, ApJS, 146, 407
Finkbeiner, D. P., Davis, M., & Schlegel, D. J. 1999, ApJ, 524, 867

Finkbeiner, D. P., Langston, G. I., & Minter, A. H. 2004, ApJ, 617, 350
Fixsen, D. J. 2009, ApJ, 707, 916
Ghosh, T., Banday, A. J., Jaffe, T., et al. 2012, MNRAS, 422, 3617
Giardino, G., Banday, A. J., Górski, K. M., et al. 2002, A&A, 387, 82
Gold, B., Odegard, N., Weiland, J. L., et al. 2011, ApJS, 192, 15
Górski, K. M., Hivon, E., Banday, A. J., et al. 2005, ApJ, 622, 759
Gould, B. A. 1879, Resultados del Observatorio Nacional Argentino, 1, D1
Haslam, C. G. T., Salter, C. J., Stoffel, H., & Wilson, W. E. 1982, A&AS, 47, 1
Hoang, T., Lazarian, A., & Draine, B. T. 2011, ApJ, 741, 87
Jarosik, N., Bennett, C. L., Dunkley, J., et al. 2011, ApJS, 192, 14
Jonas, J. L., Baart, E. E., & Nicolson, G. D. 1998, MNRAS, 297, 977
Kogut, A. 1996, in Bulletin of the American Astronomical Society, Vol. 28, American Astronomical Society Meeting Abstracts, 1295
Kogut, A., Fixsen, D. J., Levin, S. M., et al. 2011, ApJ, 734, 4
Lagache, G. 2003, A&A, 405, 813
Lamarre, J., Puget, J., Ade, P. A. R., et al. 2010, A&A, 520, A9
Leahy, J. P., Bersanelli, M., D'Arcangelo, O., et al. 2010, A&A, 520, A8
Leitch, E. M., Readhead, A. C. S., Pearson, T. J., & Myers, S. T. 1997, ApJ, 486, L23
Lindblad, P. O. 1967, Bull. Astron. Inst. Netherlands, 19, 34
Lindblad, P. O., Palous, J., Loden, K., & Lindegren, L. 1997, in ESA Special Publication, Vol. 402, Hipparcos - Venice '97, ed. R. M. Bonnet, E. Høg, P. L. Bernacca, L. Emiliani, A. Blaauw, C. Turon, J. Kovalevsky, L. Lindegren, H. Hassan, M. Bouffard, B. Strim, D. Heger, M. A. C. Perryman, & L. Woltjer, 507–512
Macellari, N., Pierpaoli, E., Dickinson, C., & Vaillancourt, J. E. 2011, MNRAS, 418, 888
Mandolesi, N., Bersanelli, M., Butler, R. C., et al. 2010, A&A, 520, A3
Mennella et al. 2011, A&A, 536, A3
Miville-Deschênes, M.-A. & Lagache, G. 2006, in Astronomical Society of the Pacific Conference Series, Vol. 357, Astronomical Society of the Pacific Conference Series, ed. L. Armus & W. T. Reach, 167
Miville-Deschênes, M.-A., Ysard, N., Lavabre, A., et al. 2008, A&A, 490, 1093
Peel, M. W., Dickinson, C., Davies, R. D., et al. 2011, ArXiv e-prints
Perrot, C. A. & Grenier, I. A. 2003, A&A, 404, 519
Pietrobon, D., Gorski, K. M., Bartlett, J., et al. 2011, ArXiv e-prints
Planck Collaboration I. 2011, A&A, 536, A1
Planck Collaboration II. 2011, A&A, 536, A2
Planck Collaboration II. 2013, Planck Collaboration II. Planck first CMB release. II. Low Frequency Instrument data processing (A&A in preparation)
Planck Collaboration IX. 2012, Planck intermediate results. IX. Detection of the Galactic haze with Planck (Submitted to A&A, [arXiv:astro-ph/1208.5483])
Planck Collaboration TBC. 2013, Planck intermediate results: A study of Anomalous Microwave Emission in Galactic clouds (A&A in preparation)
Planck Collaboration VI. 2013, Planck Collaboration VI. Planck first CMB release. VI. High Frequency Instrument data processing (A&A in preparation)
Planck Collaboration XIX. 2011, A&A, 536, A19
Planck Collaboration XX. 2011, A&A, 536, A20
Planck Collaboration XXI. 2011, A&A, 536, A21
Planck Collaboration XXV. 2011, A&A, 536, A25
Planck HFI Core Team. 2011a, A&A, 536, A4
Planck HFI Core Team. 2011b, A&A, 536, A6
Reynolds, R. J. & Ogden, P. M. 1979, ApJ, 229, 942
Ricciardi, S., Bonaldi, A., Natoli, P., et al. 2010, MNRAS, 406, 1644
Rosset, C., Tristram, M., Ponthieu, N., et al. 2010, A&A, 520, A13
Schlegel, D. J., Finkbeiner, D. P., & Davis, M. 1998, ApJ, 500, 525
Silsbee, K., Ali-Haïmoud, Y., & Hirata, C. M. 2011, MNRAS, 411, 2750
Tauber, J. A., Mandolesi, N., Puget, J., et al. 2010, A&A, 520, A1
Tegmark, M., Eisenstein, D. J., Hu, W., & de Oliveira-Costa, A. 2000, ApJ, 530, 133
Witt, A. N., Gold, B., Barnes, III, F. S., et al. 2010, ApJ, 724, 1551
Wood, K. & Reynolds, R. J. 1999, ApJ, 525, 799
Ysard, N., Juvela, M., & Verstraete, L. 2011, A&A, 535, A89
Ysard, N., Miville-Deschênes, M. A., & Verstraete, L. 2010, A&A, 509, L1
Ysard, N. & Verstraete, L. 2010, A&A, 509, A12
Zacchei et al. 2011, A&A, 536, A5

Appendix A: Harmonic-domain CCA

The sky radiation, $\tilde{x}$, from direction r at frequency ν results from the superposition of signals coming from N_c different physical processes $\tilde{s}_j$:

$$\tilde{x}(r,\nu) = \sum_{j=1}^{N_c} \tilde{s}_j(r,\nu). \tag{A.1}$$

The signal $\tilde{x}$ is observed through a telescope, the beam pattern of which can be modelled, at each frequency, as a spatially invariant point spread function $B(r,\nu)$. For each value of ν, the telescope convolves the physical radiation map with B. The frequency-dependent convolved signal is input to an N_d-channel measuring instrument, which integrates the signal over frequency for each of its channels and adds noise to its outputs. The output of the measurement channel at a generic frequency ν is

$$x_\nu(r) = \int B(r-r',\nu') \sum_{j=1}^{N_c} t_\nu(\nu')\tilde{s}_j(r',\nu')dr'd\nu' + n_\nu(r), \tag{A.2}$$

where $t_\nu(\nu')$ is the frequency response of the channel and $n_\nu(r)$ is the noise map. The data model in Eq. (A.2) can be simplified by virtue of the following assumptions:

– Each source signal is a separable function of direction and frequency, i.e.,

$$\tilde{s}_j(r,\nu) = s_j(r) f_j(\nu); \tag{A.3}$$

– $B(r,\nu) = B_\nu(r)$ is constant within the bandpass of the measurement channel.

These two assumptions lead us to a new data model:

$$x_\nu(r) = B_\nu(r) * \sum_{j=1}^{N_c} h_{\nu j} s_j(r) + n_\nu(r), \tag{A.4}$$

where $*$ denotes convolution, and

$$h_{\nu j} \equiv \int t_\nu(\nu') f_j(\nu')d\nu'. \tag{A.5}$$

For each location, r, we define:

– the N_c-vector $\boldsymbol{s}$ (sources vector) whose elements are $s_j(r)$;
– the N_d-vector $\boldsymbol{x}$ (data vector) whose elements are $x_\nu(r)$;
– the N_d-vector $\boldsymbol{n}$ (noise vector) whose elements are $n_\nu(r)$;
– the diagonal N_d-matrix B whose elements are $B_\nu(r)$;
– the $N_d \times N_c$ matrix H containing all $h_{\nu j}$ elements.

Then, we can rewrite Eq. (A.4) in vector form:

$$\boldsymbol{x}(r) = [\mathsf{B} * \mathsf{H}\boldsymbol{s}](r) + \boldsymbol{n}(r). \tag{A.6}$$

The matrix H is called the mixing matrix and contains the frequency scaling of the components for all the data maps involved.

When working in the pixel domain, under the assumption that B does not depend on the frequency, we can simplify Eq. (A.6) to

$$\boldsymbol{x} = \mathsf{H}\boldsymbol{s} + \boldsymbol{n}, \tag{A.7}$$

where the components in the source vector $\boldsymbol{s}$ are now convolved with the instrumental beam.

Eq. (A.6) can be translated to the harmonic domain, where, for each transformed mode, it becomes

$$\boldsymbol{X} = \widetilde{\mathsf{B}}\mathsf{H}\boldsymbol{S} + \boldsymbol{N}, \tag{A.8}$$

where $\boldsymbol{X}$, $\boldsymbol{S}$, and $\boldsymbol{N}$ are the transforms of $\boldsymbol{x}$, $\boldsymbol{s}$, and $\boldsymbol{n}$, respectively, and $\widetilde{\mathsf{B}}$ is the transform of matrix B. Relying on this data model we can derive the following relation between the cross-spectra of the data $\widetilde{\mathsf{C}}_{\boldsymbol{x}}(\ell)$, sources $\widetilde{\mathsf{C}}_{\boldsymbol{s}}(\ell)$ and noise, $\widetilde{\mathsf{C}}_{\boldsymbol{n}}(\ell)$, all depending on the multipole ℓ:

$$\widetilde{\mathsf{C}}_{\boldsymbol{x}}(\ell) = \widetilde{\mathsf{B}}(\ell)\mathsf{H}\widetilde{\mathsf{C}}_{\boldsymbol{s}}(\ell)\mathsf{H}^{\mathrm{T}}\widetilde{\mathsf{B}}^{\dagger}(\ell) + \widetilde{\mathsf{C}}_{\boldsymbol{n}}(\ell), \tag{A.9}$$

where the dagger superscript denotes the adjoint matrix. To reduce the number of unknowns, the mixing matrix is parametrized through a parameter vector $\boldsymbol{p}$ (such that $\mathsf{H} = \mathsf{H}(\boldsymbol{p})$), using the fact that its elements are proportional to the spectra of astrophysical sources (see Sect. 3.2).

Since the foreground properties are expected to be spatially variable, we work on relatively small square patches of data. This allows us to use the 2D Fourier transform to approximate the harmonic spectra (see, e.g., Bond & Efstathiou 1987).

The HEALPix (Górski et al. 2005) data on the sphere are projected on the plane tangential to the centre of the patch and re-gridded with a suitable number of bins in order to correctly sample the original resolution. Each pixel in the projected image is associated with a specific vector normal to the tangential plane and it assumes the value of the HEALPix pixel nearest to the corresponding position on the sphere. Clearly, the projection and re-gridding process will create some distortion in the image at small scales and will modify the noise properties. However, we verified that this has negligible impact on the spectra in Eq. (A.9) for the scales considered in this work and, therefore, on the spectral parameters. If $\boldsymbol{x}(i, j)$ contains the data projected on the planar grid and $\boldsymbol{X}(i, j)$ is its 2-dimensional discrete Fourier transform, the energy of the signal at a certain scale, which corresponds to the power spectrum, can be obtained as the average of $\boldsymbol{X}(i, j)\boldsymbol{X}^{\dagger}(i, j)$ over annular bins $D_{\hat{\ell}}$, $\hat{\ell} = 1, \ldots, \hat{\ell}_{\max}$ (Bedini & Salerno 2007):

$$\widetilde{\mathsf{C}}_{\mathsf{x}}(\hat{\ell}) = \frac{1}{M_{\hat{\ell}}} \sum_{i,j \in D_{\hat{\ell}}} \boldsymbol{X}(i, j)\boldsymbol{X}^{\dagger}(i, j), \tag{A.10}$$

where $M_{\hat{\ell}}$ is the number of pairs (i, j) contained in the spectral bin denoted by $D_{\hat{\ell}}$. Every spectral bin $\hat{\ell}$ is related to a specific ℓ in the spherical harmonic domain by

$$\ell = (\hat{\ell} - 1)\, 2p\Delta_{\ell}/N_{\mathrm{pix}} \tag{A.11}$$

where p is the thickness of the annular bin, $\Delta_{\ell} = 180/L_{\mathrm{deg}}\,(N_{\mathrm{pix}} - 1)$, and L_{deg}, N_{pix} are the size in degrees and the number of pixels on the side of the square patch, respectively.

If we reorder the matrices $\mathsf{C}_{\boldsymbol{x}}(\hat{\ell}) - \mathsf{C}_{\boldsymbol{n}}(\hat{\ell})$ and $\mathsf{C}_{\boldsymbol{s}}(\hat{\ell})$ into vectors $\boldsymbol{d}(\hat{\ell})$ and $\boldsymbol{c}(\hat{\ell})$, respectively, we can rewrite Eq. (A.9) as

$$\boldsymbol{d}(\hat{\ell}) = \mathsf{H}_k(\hat{\ell})\boldsymbol{c}(\hat{\ell}) + \boldsymbol{\epsilon}(\hat{\ell}), \tag{A.12}$$

where $\mathsf{H}_k(\hat{\ell}) = [\widetilde{\mathsf{B}}(\hat{\ell})\mathsf{H}] \otimes [\widetilde{\mathsf{B}}(\hat{\ell})\mathsf{H}]$, and the symbol $\otimes$ denotes the Kronecker product. The vector $\boldsymbol{d}(\hat{\ell})$ is now computed using the approximated data cross-spectrum matrix in Eq. (A.10) and $\boldsymbol{\epsilon}(\hat{\ell})$ represents the error on the noise power spectrum.

The parameter vector $\boldsymbol{p}$ and the source cross-spectra are finally obtained by minimizing the functional:

$$\boldsymbol{\Phi}[\boldsymbol{p}, \boldsymbol{c}_V] = \tag{A.13}$$
$$[\boldsymbol{d}_V - \mathsf{H}_{kB}(\boldsymbol{p}) \cdot \boldsymbol{c}_V]^T \mathsf{N}_{\epsilon B}^{-1}[\boldsymbol{d}_V - \mathsf{H}_{kB}(\boldsymbol{p}) \cdot \boldsymbol{c}_V] + \lambda \boldsymbol{c}_V^{\mathrm{T}}\mathsf{C}\boldsymbol{c}_V.$$

The vectors $\boldsymbol{d}_V$ and $\boldsymbol{c}_V$ contain the elements $\boldsymbol{d}(\hat{\ell})$ and $\boldsymbol{c}(\hat{\ell})$, respectively, and the diagonal matrices H_{kB} and N_{ϵ} the elements $\mathsf{H}_k(\hat{\ell})$ and the covariance of error $\boldsymbol{\epsilon}(\hat{\ell})$ for all the relevant spectral bins. The term $\lambda \boldsymbol{c}_V^{\mathrm{T}}\mathsf{C}\boldsymbol{c}_V$ is a quadratic stabilizer for the source power cross-spectra: the matrix C is in our case the identity matrix, and the parameter λ must be tuned to balance the effects of data fit and regularization in the final solution. The functional in Eq. (A.13) can be considered as a negative joint log-posterior for $\boldsymbol{p}$ and $\boldsymbol{c}_V$, where the first quadratic form represents the log-likelihood, and the regularization term can be viewed as a log-prior density for the source power cross-spectra.

Appendix B: Spectral model for AME

Theoretical spinning dust models predict a variety of spectra, which can be substantially different in shape, depending on a large number of parameters describing the physics of the medium. The number of such physical parameters is too large to be constrained by the data in the available frequency range. For the purpose of the estimation of the spectral behaviour of the AME we adopt a simple formula depending on only a few parameters. The CCA component separation method used in this work implements the parametric relation proposed by Bonaldi et al. (2007) [Eq. (6)], depending on the peak frequency, ν_{p}, and slope at 60 GHz, m_{60}. To verify the adequacy of this parametrization we produced spinning dust spectra for different input physical parameters with the `SpDust` code and fitted each of them with the proposed relation by minimizing the χ^2 for the set of frequencies used in this work. The input models we consider are: weak neutral medium (WNM); cold neutral medium (CNM); weak ionized medium (WIM); and molecular cloud (MC). Both the input `SpDust` parameters and the best-fit m_{60}, ν_{p} parameters for each model are reported in Table B.1. For comparison, we also consider alternative parametric relations and in particular:

- the model implemented in the `Commander` component separation method (Pietrobon et al. 2011, Planck Collaboration IX 2012) which is a Gaussian in the $T_{\mathrm{CMB}} - \ln(\nu)$ plane, parametrized in terms of central frequency and width;
- the Tegmark et al. (2000) model, which is a modified blackbody relation [Eq. (1)] having temperature around 0.25 K and emissivity index around 2.4;

As this test does not account for the presence of the other components and does not include any data simulation, it verifies the intrinsic ability of the parametric model to reproduce the actual spectra. Realistic estimation errors for the CCA model are derived through simulations in Appendix C.

Fig. B.1 compares the input spectra with the best-fit models for the different parametrizations. In general, the fits are accurate at least up to $\nu = 50$–60 GHz, while at higher frequencies the parametric relations may not be able to reproduce the input spectra in detail. This is a consequence of fitting complex spectra with only a few parameters. The fit tends to fail where the AME signal is weaker.

Over the frequency range considered, CCA and `Commander` models fit the input spectrum generally better than the Tegmark et al. (2000) model (which falls off too rapidly at high frequencies). When adding lower frequency data, however, CCA and `Commander` models will be increasingly inaccurate, as they are symmetric with respect to the peak of the emission. The models implemented by CCA and `Commander` perform quite similarly, despite the different formulation. As a result, those methods are able to give consistent answers, which ensures consistency between different analyses within *Planck* (e.g. Planck Collaboration IX 2012).

The CCA model used in this work provides a reasonable fit to theoretical spinning dust models for a variety of physical

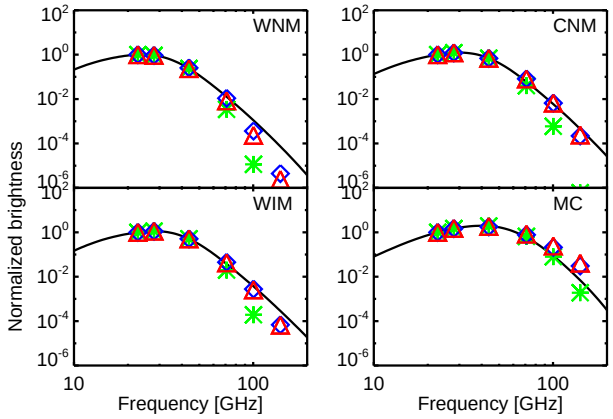

Fig. B.1. Theoretical spinning dust models produced with `SpDust` (solid lines) and fitted with CCA (triangles), `Commander` (diamonds), and Tegmark et al. (2000) (asterisks) models. Input `SpDust` parameters and best-fit parameters for the CCA model are provided in Table B.1.

conditions. The best-fit parameters that we obtain, reported in Table B.1, vary significantly from one input model to another and have a straightforward interpretation in terms of the spectrum.

Appendix C: Description of the simulations

We simulated *Planck* and *WMAP* 7-yr data by assuming monochromatic bandpasses positioned at the central frequency of the bands, Gaussian beams at the nominal values indicated in Tables 1 and 2, and Gaussian noise generated according to realistic, spatially varying noise RMS. Our model of the sky consists of the following components:

- CMB emission given by the best-fit power spectrum model from *WMAP* 7-yr analyses;
- synchrotron emission given by the Haslam et al. (1982) template scaled in frequency with a power-law model with a spatially varying synchrotron spectral index β_s, as modelled by Giardino et al. (2002);
- free-free emission given by the Dickinson et al. (2003) Hα corrected for dust absorption with the $E(B-V)$ map from Schlegel et al. (1998) with a dust absorption fraction f_d = 0.33, and scaled in frequency according to Eq. (2) with T_e = 7000 K;
- thermal dust emission modelled with the 100 μm map from Schlegel et al. (1998), scaled in frequency according to Eq. (1) with T_d = 18 K and a spatially varying β_d having average value of 1.7;
- AME modelled by the $E(B-V)$ map from Schlegel et al. (1998) with intensity at 23 GHz calibrated using the results of Ghosh et al. (2012) for the same region of the sky.

We adopted more than one spectral model for the AME. We first considered two convex spectra, generated with the `SpDust` code: one peaking around 26 GHz and the other peaking around 19 GHz. We also tested a spatially varying power-law model (with spectral index of -3.6 ± 0.6, Ghosh et al. 2012), which could result from the superposition of multiple convex components along the line of sight.

It is worth noting that the simulated sky is more complex than the model assumed in the component separation. This has been done intentionally, to reflect a more realistic situation. Another realistic feature we included is the presence of errors in the synchrotron and free-free templates. The spatial variability of the synchrotron spectral index modifies the morphology of the component with respect to that traced by the 408 MHz map from Haslam et al. (1982). The use of Hα as a tracer of free-free emission is affected by even larger uncertainties. Our uncertainties on the dust absorption fraction f_d (estimated to be $f_d = 0.33^{+0.10}_{-0.15}$ at intermediate latitudes by Dickinson et al. 2003) and on the scattering of Hα photons from dust grains, can create dust-correlated biases in the template. This is illustrated in Fig. C.1, where we compare different versions of the free-free template. $\mathrm{FF_{REF}}$ is our reference template, adopted for the analysis of real data and for simulating the component, which is corrected for f_d = 0.33 as described in Dickinson et al. (2003). Two more templates ($\mathrm{FF_1}$ and $\mathrm{FF_2}$) have been obtained by correcting Hα for $f_d = 0.33 - 0.15$ and $f_d = 0.33 + 0.1$ ($\pm 1\sigma$ according to Dickinson et al. 2003). A final template ($\mathrm{FF_3}$) has been obtained by correcting $\mathrm{FF_{REF}}$ for scattered light at the 15 % level by subtracting from the free-free map the 1 μm map of Schlegel et al. (1998) multiplied by a suitable constant factor (Witt et al. 2010). Difference maps $(\mathrm{FF_i} - \mathrm{FF_{REF}})/\mathrm{FF_{REF}}$, presented in the lower panels of Fig. C.1, are on average of order of 10 %, but can be much higher (up to 50–60 %) in regions of strong dust emission.

When analysing the simulated data, we used both $\mathrm{FF_1}$ and $\mathrm{FF_2}$ as free-free templates in place of $\mathrm{FF_{REF}}$, which corresponds to the simulated component. For synchrotron emission the morphological mismatch between the simulated component and the template has been achieved by scaling the component from 23 GHz to 408 MHz with a spatially varying spectral index. The comparison between component and template is presented in Fig. C.2; the differences are of the order of 10 %. The simulated data-sets described above have been analysed with the CCA method using the same procedure applied to the real data; the results of this assessment are presented in Sect. 4.1. As a separate test, we verified the impact of the CMB component on the results for ν_p and m_{60}. We generated 100 sets of mock data having the same foreground emission and different realizations of CMB and instrumental noise, and repeated the estimation of the AME frequency scaling. For this test we used the simulation with a spatially constant AME spectrum peaking at 26 GHz. As this analysis is computationally demanding, the CCA estimation has been performed only on the 10 independent patches covering the Gould Belt region (centred on latitudes $-20°$ and $-40°$ and longitudes of 140°, 160°, 180°, 200°, and 220°). In Fig. C.3 we show the average (diamonds) and RMS (error bars) ν_p and m_{60} over the 100 realizations for each patch, for different patches on the x-axis. The scatter between the results obtained for different patches (indicated by the grey area in the plots) is typically larger than the error bars, measuring the scatter due to different CMB realizations. This means that the foreground emission generally dominates over the CMB as a source of error. Larger error bars associated with the CMB are obtained for three patches having fainter foreground emission. For such patches the estimated errors on ν_p and m_{60} are consistently larger. The CMB variation results on average in $\Delta\nu_p$ = 0.1 GHz and Δm_{60} = 0.3, which reach 0.3 GHz and 0.8, respectively, for the worst sky patch. Those values are below the error bars resulting from the analysis of the data, which amount to 1–1.5 GHz for ν_p and 1.5–2 for m_{60}. The CMB has limited impact on the results because this component is modelled in the mixing matrix. Having a known frequency scaling, the statistical constraint used by CCA is able to trace the

Table B.1. Spdust input parameters for the spectra in Fig. B.1 and best-fit parameters for the CCA spectral model.

	SpDust					CCA	
model name	nH [cm-3]	T[K]	χ	x_H	x_C	ν_p	m_{60}
WNM	0.4	6000	1.00	0.10	0.0003	24.22	7.53
CNM	30.0	100	1.00	0.0012	0.0003	29.00	4.93
WIM	0.1	8000	1.00	0.99	0.001	27.30	5.66
MC	300	20	0.01	0.0	0.0001	38.77	2.00

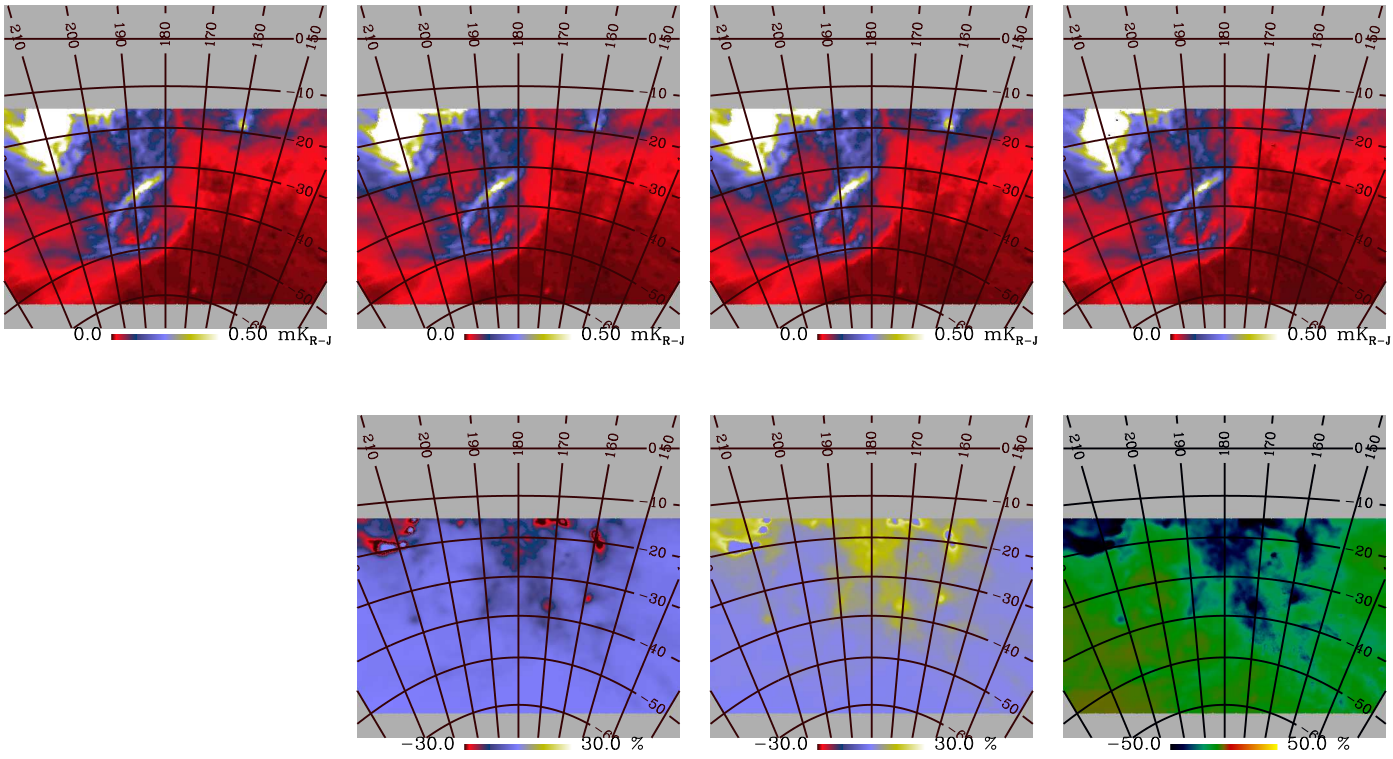

Fig. C.1. Free-free templates at 23 GHz used for the analysis. The reference template FF_{REF} is in the upper left corner; the other columns (left to right) are FF_1, FF_2 and FF_3, respectively. The differences in the lower panels $(FF_i - FF_{REF})/FF_{REF}$ are on average of the order of 10 %, but reach 50 % in regions of strong dust emission.

pattern of the CMB through the frequencies with good precision and hence identify it correctly.

[1] APC, AstroParticule et Cosmologie, Université Paris Diderot, CNRS/IN2P3, CEA/lrfu, Observatoire de Paris, Sorbonne Paris Cité, 10, rue Alice Domon et Léonie Duquet, 75205 Paris Cedex 13, France
[2] Aalto University Metsähovi Radio Observatory, Metsähovintie 114, FIN-02540 Kylmälä, Finland
[3] African Institute for Mathematical Sciences, 6-8 Melrose Road, Muizenberg, Cape Town, South Africa
[4] Agenzia Spaziale Italiana Science Data Center, c/o ESRIN, via Galileo Galilei, Frascati, Italy
[5] Agenzia Spaziale Italiana, Viale Liegi 26, Roma, Italy
[6] Astrophysics Group, Cavendish Laboratory, University of Cambridge, J J Thomson Avenue, Cambridge CB3 0HE, U.K.
[7] CITA, University of Toronto, 60 St. George St., Toronto, ON M5S 3H8, Canada
[8] CNR - ISTI, Area della Ricerca, via G. Moruzzi 1, Pisa, Italy
[9] CNRS, IRAP, 9 Av. colonel Roche, BP 44346, F-31028 Toulouse cedex 4, France
[10] California Institute of Technology, Pasadena, California, U.S.A.
[11] Centre of Mathematics for Applications, University of Oslo, Blindern, Oslo, Norway
[12] Centro de Estudios de Física del Cosmos de Aragón (CEFCA), Plaza San Juan, 1, planta 2, E-44001, Teruel, Spain
[13] Computational Cosmology Center, Lawrence Berkeley National Laboratory, Berkeley, California, U.S.A.
[14] Consejo Superior de Investigaciones Científicas (CSIC), Madrid, Spain
[15] DSM/Irfu/SPP, CEA-Saclay, F-91191 Gif-sur-Yvette Cedex, France
[16] DTU Space, National Space Institute, Technical University of Denmark, Elektrovej 327, DK-2800 Kgs. Lyngby, Denmark
[17] Département de Physique Théorique, Université de Genève, 24, Quai E. Ansermet,1211 Genève 4, Switzerland
[18] Departamento de Física Fundamental, Facultad de Ciencias, Universidad de Salamanca, 37008 Salamanca, Spain
[19] Departamento de Física, Universidad de Oviedo, Avda. Calvo Sotelo s/n, Oviedo, Spain
[20] Department of Astrophysics/IMAPP, Radboud University Nijmegen, P.O. Box 9010, 6500 GL Nijmegen, The Netherlands

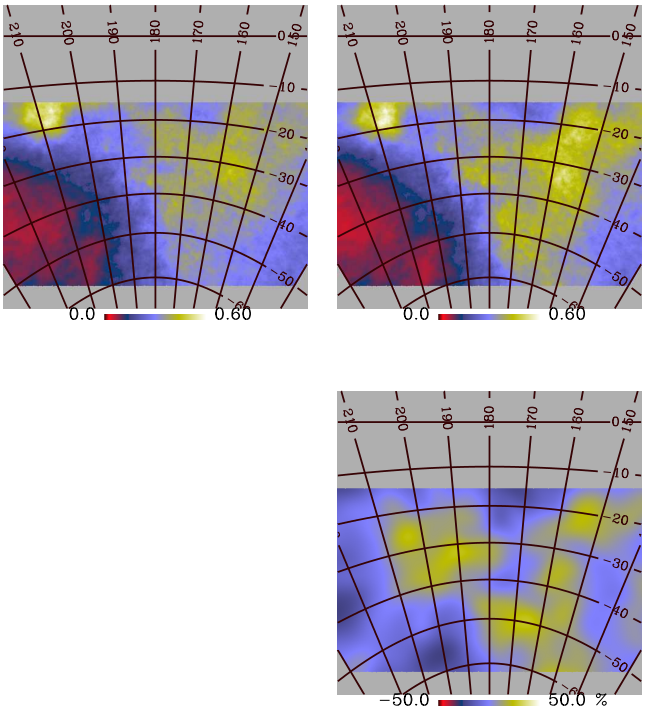

Fig. C.2. *Upper panel*: simulated synchrotron component (left) and synchrotron template (right) at 23 GHz. *Lower panel*: difference map divided by the simulated component.

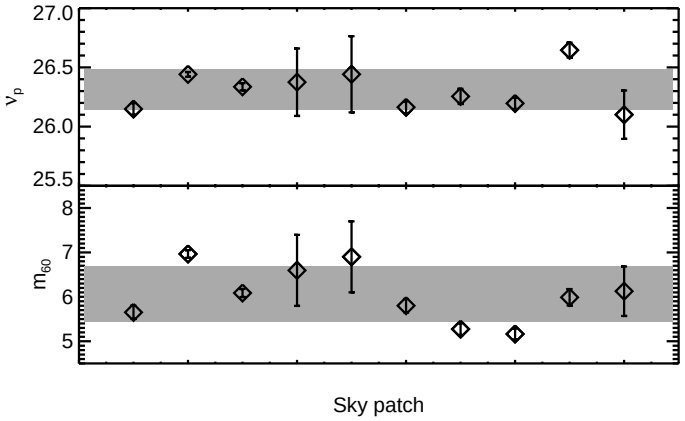

Fig. C.3. Average and RMS of v_p and m_{60} estimated over simulations having different CMB and noise realizations for different patches on the *x*-axis. The grey area is the average and RMS over different patches, which is typically larger than that due to noise and CMB.

[21] Department of Electrical Engineering and Computer Sciences, University of California, Berkeley, California, U.S.A.
[22] Department of Physics & Astronomy, University of British Columbia, 6224 Agricultural Road, Vancouver, British Columbia, Canada
[23] Department of Physics and Astronomy, Dana and David Dornsife College of Letter, Arts and Sciences, University of Southern California, Los Angeles, CA 90089, U.S.A.
[24] Department of Physics, Gustaf Hällströmin katu 2a, University of Helsinki, Helsinki, Finland
[25] Department of Physics, University of California, Santa Barbara, California, U.S.A.
[26] Department of Physics, University of Illinois at Urbana-Champaign, 1110 West Green Street, Urbana, Illinois, U.S.A.
[27] Dipartimento di Fisica e Astronomia G. Galilei, Università degli Studi di Padova, via Marzolo 8, 35131 Padova, Italy
[28] Dipartimento di Fisica e Scienze della Terra, Università di Ferrara, Via Saragat 1, 44122 Ferrara, Italy
[29] Dipartimento di Fisica, Università La Sapienza, P. le A. Moro 2, Roma, Italy
[30] Dipartimento di Fisica, Università degli Studi di Milano, Via Celoria, 16, Milano, Italy
[31] Dipartimento di Fisica, Università degli Studi di Trieste, via A. Valerio 2, Trieste, Italy
[32] Dipartimento di Fisica, Università di Roma Tor Vergata, Via della Ricerca Scientifica, 1, Roma, Italy
[33] Discovery Center, Niels Bohr Institute, Blegdamsvej 17, Copenhagen, Denmark
[34] Dpto. Astrofísica, Universidad de La Laguna (ULL), E-38206 La Laguna, Tenerife, Spain
[35] European Space Agency, ESAC, Planck Science Office, Camino bajo del Castillo, s/n, Urbanización Villafranca del Castillo, Villanueva de la Cañada, Madrid, Spain
[36] European Space Agency, ESTEC, Keplerlaan 1, 2201 AZ Noordwijk, The Netherlands
[37] Helsinki Institute of Physics, Gustaf Hällströmin katu 2, University of Helsinki, Helsinki, Finland
[38] INAF - Osservatorio Astronomico di Padova, Vicolo dell'Osservatorio 5, Padova, Italy
[39] INAF - Osservatorio Astronomico di Roma, via di Frascati 33, Monte Porzio Catone, Italy
[40] INAF - Osservatorio Astronomico di Trieste, Via G.B. Tiepolo 11, Trieste, Italy
[41] INAF Istituto di Radioastronomia, Via P. Gobetti 101, 40129 Bologna, Italy
[42] INAF/IASF Bologna, Via Gobetti 101, Bologna, Italy
[43] INAF/IASF Milano, Via E. Bassini 15, Milano, Italy
[44] INFN, Sezione di Bologna, Via Irnerio 46, I-40126, Bologna, Italy
[45] INFN, Sezione di Roma 1, Universit'a di Roma Sapienza, Piazzale Aldo Moro 2, 00185, Roma, Italy
[46] IUCAA, Post Bag 4, Ganeshkhind, Pune University Campus, Pune 411 007, India
[47] Imperial College London, Astrophysics group, Blackett Laboratory, Prince Consort Road, London, SW7 2AZ, U.K.
[48] Infrared Processing and Analysis Center, California Institute of Technology, Pasadena, CA 91125, U.S.A.
[49] Institut Néel, CNRS, Université Joseph Fourier Grenoble I, 25 rue des Martyrs, Grenoble, France
[50] Institut Universitaire de France, 103, bd Saint-Michel, 75005, Paris, France
[51] Institut d'Astrophysique Spatiale, CNRS (UMR8617) Université Paris-Sud 11, Bâtiment 121, Orsay, France
[52] Institut d'Astrophysique de Paris, CNRS (UMR7095), 98 bis Boulevard Arago, F-75014, Paris, France
[53] Institute for Space Sciences, Bucharest-Magurale, Romania
[54] Institute of Astronomy and Astrophysics, Academia Sinica, Taipei, Taiwan
[55] Institute of Astronomy, University of Cambridge, Madingley Road, Cambridge CB3 0HA, U.K.
[56] Institute of Theoretical Astrophysics, University of Oslo, Blindern, Oslo, Norway
[57] Instituto de Astrofísica de Canarias, C/Vía Láctea s/n, La Laguna, Tenerife, Spain
[58] Instituto de Física de Cantabria (CSIC-Universidad de Cantabria), Avda. de los Castros s/n, Santander, Spain
[59] Jet Propulsion Laboratory, California Institute of Technology, 4800 Oak Grove Drive, Pasadena, California, U.S.A.

[60] Jodrell Bank Centre for Astrophysics, Alan Turing Building, School of Physics and Astronomy, The University of Manchester, Oxford Road, Manchester, M13 9PL, U.K.
[61] Kavli Institute for Cosmology Cambridge, Madingley Road, Cambridge, CB3 0HA, U.K.
[62] Kavli Institute for Theoretical Physics, University of California, Santa Barbara Kohn Hall, Santa Barbara, CA 93106, U.S.A.
[63] LAL, Université Paris-Sud, CNRS/IN2P3, Orsay, France
[64] LERMA, CNRS, Observatoire de Paris, 61 Avenue de l'Observatoire, Paris, France
[65] Laboratoire AIM, IRFU/Service d'Astrophysique - CEA/DSM - CNRS - Université Paris Diderot, Bât. 709, CEA-Saclay, F-91191 Gif-sur-Yvette Cedex, France
[66] Laboratoire de Physique Subatomique et de Cosmologie, Université Joseph Fourier Grenoble I, CNRS/IN2P3, Institut National Polytechnique de Grenoble, 53 rue des Martyrs, 38026 Grenoble cedex, France
[67] Laboratoire de Physique Théorique, Université Paris-Sud 11 & CNRS, Bâtiment 210, 91405 Orsay, France
[68] Lawrence Berkeley National Laboratory, Berkeley, California, U.S.A.
[69] Max-Planck-Institut für Astrophysik, Karl-Schwarzschild-Str. 1, 85741 Garching, Germany
[70] MilliLab, VTT Technical Research Centre of Finland, Tietotie 3, Espoo, Finland
[71] National University of Ireland, Department of Experimental Physics, Maynooth, Co. Kildare, Ireland
[72] Niels Bohr Institute, Blegdamsvej 17, Copenhagen, Denmark
[73] Optical Science Laboratory, University College London, Gower Street, London, U.K.
[74] SISSA, Astrophysics Sector, via Bonomea 265, 34136, Trieste, Italy
[75] School of Physics and Astronomy, Cardiff University, Queens Buildings, The Parade, Cardiff, CF24 3AA, U.K.
[76] Space Sciences Laboratory, University of California, Berkeley, California, U.S.A.
[77] Special Astrophysical Observatory, Russian Academy of Sciences, Nizhnij Arkhyz, Zelenchukskiy region, Karachai-Cherkessian Republic, 369167, Russia
[78] Stanford University, Dept of Physics, Varian Physics Bldg, 382 Via Pueblo Mall, Stanford, California, U.S.A.
[79] UPMC Univ Paris 06, UMR7095, 98 bis Boulevard Arago, F-75014, Paris, France
[80] Université de Toulouse, UPS-OMP, IRAP, F-31028 Toulouse cedex 4, France
[81] Universities Space Research Association, Stratospheric Observatory for Infrared Astronomy, MS 211-3, Moffett Field, CA 94035, U.S.A.
[82] University of Granada, Departamento de Física Teórica y del Cosmos, Facultad de Ciencias, Granada, Spain
[83] University of Miami, Knight Physics Building, 1320 Campo Sano Dr., Coral Gables, Florida, U.S.A.
[84] Warsaw University Observatory, Aleje Ujazdowskie 4, 00-478 Warszawa, Poland